Hindawi
Journal of Nanomaterials
Volume 2021, Article ID 7475902, 21 pages
https://doi.org/10.1155/2021/7475902

Research Article

Surface Roughness and Electrochemical Performance Properties of Biosynthesized α-MnO_2/NiO-Based Polyaniline Ternary Composites as Efficient Catalysts in Microbial Fuel Cells

Yilkal Dessie,[1] **Sisay Tadesse**,[2] **and Rajalakshmanan Eswaramoorthy**[1]

[1]*Department of Applied Chemistry, Adama Science and Technology University, Adama, Ethiopia*
[2]*Chemistry Department, Hawassa University, Hawassa, Ethiopia*

Correspondence should be addressed to Yilkal Dessie; yilikaldessie@gmail.com

Received 7 May 2021; Revised 2 June 2021; Accepted 4 June 2021; Published 30 June 2021

Academic Editor: Ibrahim Alarifi

In this study, biosynthesized α-MnO_2/NiO NPs and chemically oxidative polyaniline (PANI) were synthesized to form ternary composite anode material for MFC. The synthesized materials were characterized with different materials (UV-Vis, FTIR, XRD, TGA-DTA-DSC, SEM-EDX-Gwyddion, CV, and EIS) to deeply examine their optical, structural, morphological, thermal, roughness, and electrocatalytic properties. The degree of surface roughness for α-MnO_2/NiO/PANI was 23.65 ± 5.652 nm. This value was higher than the pure α-MnO_2, pure PANI, and even α-MnO_2/PANI nanocomposite due to surface modification. The total charge storing performance for bare PGE, α-MnO_2/PGE, PANI/PGE, α-MnO_2/PANI/PGE, and α-MnO_2/NiO/PANI/PGE were 5.291, 17.267, 20.659, 23.258, and 24.456 mC. From this, the charge storing performance formed by α-MnO_2/NiO/PANI-modified PGE was highest, indicating that this electrode is best in cycle stability and increases its life cycle during energy conversion time in MFC. This is also supported by its effective surface area, having a value of 0.00984 cm^2. From this, it is evidenced that the ternary composite catalyst-modified anode facilitates the fast electrocatalytic activity as observed from its high peak current and lower peak-to-peak potential separation ($\Delta E_p = 0.216$ V) than other electrodes. Such surface modification helps to store more electrical charge by increasing electrical conductivity during its charge/discharge processing time. In addition, the lower charge transfer resistance property with a value of 788.9 Ω and the fast heterogeneous electron transfer rate of ~2.92 s^{-1} enable to facilitate glucose oxidation, and this enhances to produce high power output and increase wastewater treatment efficiency. As a result, the bioelectrical activity of α-MnO_2/NiO/PANI composite-modified PGE was very effective in producing a maximum power density of 506.96 mW m^{-2} with COD of 81.92%. The above observations justified that α-MnO_2/NiO/PANI/PGE serves as an effective anode material in double-chambered MFC application.

1. Introduction

Focusing on alternative, renewable, and carbon-neutral energy sources produced by the bioelectrochemical system is necessary to keep the environment from pollution and economic sustainability across the globe [1]. Due to this, the microbial fuel cell (MFC) is chosen as the more affordable device that enables to produce renewable electrical energy followed by simultaneous wastewater treatment [1]. Therefore, the way to produce renewable energy from organic effluents and green treatments of liquid wastes has received much attention in MFC [2]. The device is able to produce renewable bioelectricity from stored chemicals found on organic pollutants in the presence of electroactive microorganisms (EAM) [3, 4]. But the low power output, poor stability, and cost-ineffectiveness to upgrade the device are the main drawbacks that affect MFC [2]. This is due to the low electron transfer rate and low EAM attachment found on electrode components [5]. Electrodes from conventional carbon materials are the most common but are poor in energy conversion and low in wastewater treatment efficiency due to the short-term stability results for sluggish electron transfer rates between electrodes and EAM [6]. This limitation in general affects the whole performance of MFC.

To reduce these challenges, researchers have used transition metal oxide- (TMO-) based nanomaterial catalysts to modify such conventional carbon electrodes due to their low cost, environmentally friendly nature, abundance, high surface area to volume ratio, and fast electrokinetic activity in a widespread of electrochemical applications [7]. However, due to their poor electrical conductivity, poor dispersibility, and low stability in highly protonic media, they reduce their long-term electrocatalytic activity in bioenergy production (i.e., reduces the life cycle), bioremediation, and sensing activity [3, 7]. Improving the electrochemical properties of TMO by forming a composite with conducting polymers enables to increase the life cycle of the modified electrode by improving its cycle stability in any energy conversion and storage applications. So, conducting polymers like PANI modify anodes by enhancing their electrical conductivity and surface areas when they form composites [8]. However, PANI lowers the electrochemical electrocatalytic activity and life cycle of the anode electrode in the MFC device under neutral conditions during its charge/discharge processing time. Not only this, the swelling and shrinkage behavior of PANI affects the physical strength of the bioanode while TMO NPs have a significant achievement to increase the cycle stability by increasing the specific capacitance of conventional carbon electrodes by forming composites under near-neutral and neutral solutions [9]. This is due to the finding of high theoretical capacitance on TMO and is considered a good option for anode modifier nanocatalysts when they form nanocomposites due to efficiency and stability improvement [10].

So, researchers usually combined different TMO with conducting polymers to modify conventional carbon material properties such as electrical conductivity, compatibility, and dispersibility [11–13]. As an advance, electrical conductivity, biocompatibility, high surface area, and surface roughness are the main requirement for bacterial attachment in MFC anodes [14]. So, when conventional carbon electrodes were modified with nanocomposite catalysts, their electrochemical catalytic property, durability, stability, and porosity requirements should successfully meet by improving the surface area. Such improvement facilitates fast extracellular electron transfer efficiency between EAM and anodes by forming a conductive immobilization matrix [15]. Immobilization of EAM helps to enhance the close contact between bacterial cells and electrode surfaces. So, the fabricated composite catalyst could act as a bridge to fasten electron movement across MFC. Simultaneously, the unique biocompatibility property of PANI could help to reduce extracellular electron transfer resistance in MFC [3], but this activity is restricted in the near-neutral and neutral media due to its swelling and shrinkage behavior [16].

To solve all limitations stated above and to be effective in MFC performance, some TMO NP-based hybrid composites which were synthesized by different methods were used as a good electrode modifier nanocatalyst. MnO_2/polypyrrole [2, 17], MnO_2/PANI/MnO_2 [18], MnO_2/polypyrrole/MnO_2 [19], and multiwalled carbon nanotubes/MnO_2/polypyrrole [20] were studied. From those studies, their ease of synthesis was time-consuming; the use of expensive chemicals with environmentally intolerable solvents that might affect environmental safety, use of expensive synthesis instruments, lower efficiency in wastewater treatment and power output, and inefficient charge storing ability give the intention to extend this work on biosynthesized α-MnO_2/NiO-integrated conductive PANI ternary composites for MFC applications. The synthesis of α-MnO_2/NiO binary hybrids which were dispersed in the PANI matrix followed the green method. This was cost-effective and could enable to reduce expensive and toxic reducing chemical constituents because the plant extracts are an effective reducing and stabilizing agent to synthesize TMO-based nanomaterials. Therefore, finding a simple, cost-effective, and environmentally friendly green method is one of the core objectives of this study.

So, in this study, α-MnO_2/NiO/PANI ternary nanocomposites were prepared by integrating the green method with cost-effective biosynthesized α-MnO_2/NiO in a conductive PANI matrix. Hydrothermal, solvothermal, electrodeposition, electropolymerization, microwave-assisted, and pyrolysis methods were time-consuming and used expensive advanced instruments. Previously, we prepared Mn-Ni oxide bimetallic NPs by following the simple green method by using *Vernonia amygdalina* leaf extract as a reducing and stabilizing agent [21]. To be an effective nanocatalyst towards bioelectricity and its simultaneous waste remediation, the catalyst should be best in roughness degree and be efficient in electrocatalytic activities that enable to increase anode electrode performance for effective organic wastewater oxidation (i.e., facilitating substrate oxidation). Therefore, the combined α-MnO_2/NiO/PANI nanocomposite has the best surface roughness with efficient electrochemical properties than other catalysts. This was clearly modified to a conventional pencil graphite electrode (PGE) evidenced from double-chambered MFC construction.

2. Materials and Methods

2.1. Materials. Permanganate $KMnO_4$ (99%, Alpha Chemika), hydrated nickel chloride $NiCl_2{\cdot}6H_2O$ (99.99%, Merck), aniline $C_6H_5NH_2$ (99.5%, Merck), ammonium persulfate $(NH_4)_2S_2O_8$ (98%, Sigma-Aldrich), ethanol C_2H_5OH (98%, Merck), and hydrochloric acid HCl (37%, Merck) chemicals were used as received. The chemicals, nutrients, and substrates which were applicable for MFC are of analytical grade, and distilled water was used to prepare all required solutions.

2.2. Material Synthesis. An optimized α-MnO_2/NiO binary composite was prepared based on our previous method [21]. In detail, an aqueous nickel ion concentration of ~51% (*v*/*v*) to $KMnO_4$ was added in a round-bottom flask which was placed on a controlled hot plate at a fixed temperature of 80°C and fixed pH ~8 with continuous stirring. After 15 minutes, ~75% (*v*/*v*) of *V. amygdalina* leaf extract was added dropwise in the given mixture. The reaction mixture was then waited for ~25 minutes of stirring. Due to these, the speed of the stirrer was reduced due to thick dark brown precipitate formation. The obtained precipitate was centrifuged at 4000 rpm for 15 minutes. Recovered precipitates

were washed several times with distilled water and absolute ethanol to remove organic contaminants. The 4-hour hot air oven-dried precipitate was calcined at 450°C for 2 hours to give α-MnO_2/NiO bimetallic NPs. For the biosynthesized α-MnO_2 NP preparation, refer to our previous work [22].

PANI was polymerized chemically based on the literature [23] as follows. Firstly, 1 M aqueous HCl solution was mixed with 0.5 mL aniline in a round-bottom flask and stirred for 30 minutes. Secondly, 5.71 g of ammonium persulfate (APS) was dissolved in 50 mL distilled water and kept for 1 hour each. Finally, two solutions were mixed and stirred at room temperature until a dark green precipitate was formed and waited for 4 hours to polymerize. The final precipitate was washed with 0.2 M HCl solution until the filtrate becomes clear, then with ethanol to remove the monomer and oligomer and with distilled water to remove the remaining acid. The final powder was then dried in an oven at 60°C for 24 hours.

A typical *in situ* oxidative polymerization method was used to synthesize α-MnO_2/PANI binary nanocomposites by using the literature with little modification [11]. In brief, 0.5 mL aniline was dissolved in 100 mL of 1 M HCl by using a glass round-bottom flask. The mixture was waited for 30 minutes, followed by stirring. Then, 0.5 g of optimized biosynthesized α-MnO_2 NPs [22] was dispersed in 25 mL distilled water, and the mixture was exposed for 5 minutes of ultrasonication to disperse the biosynthesized material. Finally, the dispersed α-MnO_2 NPs were added dropwise to aniline hydrochloride solution with 2.86 g of 50 mL APS (oxidant and codopant) at room temperature and stirred for 4 hours to complete the polymerization. The mixture changed in color, and the obtained precipitate was collected and washed with 0.2 M HCl solution until the filtrate becomes clear, then with ethanol to remove the monomer and oligomer as well as with distilled water to remove the remaining acid. Finally, the product was dried in an oven at 60°C for 24 hours to give α-MnO_2/PANI nanocomposites.

A typical *in situ* chemical oxidative method was used to prepare α-MnO_2/NiO/PANI ternary composites based on the literature with little modification [11]. Briefly, 0.5 g of homogenously suspended α-MnO_2/NiO bimetallic NPs was dispersed in aniline hydrochloride aqueous solution (0.1 M aniline + 1 M HCl (dopant) + 1.43 g of 50 mL APS (codopant)). The mixture was stirred continuously for 4 hours to complete the polymerization reaction. The final deep dark green precipitate was then collected by filtration and washed with 0.2 M HCl solution until the filtrate becomes clear, then with ethanol several times to remove the monomer and oligomer as well as with distilled water several times to remove the acid. Finally, the product was dried in an oven at 60°C for 24 hours to give α-MnO_2/NiO/PANI nanocomposites.

2.3. Electrode Fabrication. Catalyst-modified electrodes were carried out by following the literature [24] as follows. Briefly, α-MnO_2, PANI, α-MnO_2/PANI, and α-MnO_2/NiO/PANI were dispersed with polyvinyl alcohol (PVOH, MW = 44.05 g mol^{-1}) polymer binder solution in the ratio of 1 : 5 (PVOH to NPs, wt/wt%). Before coating, the mixture was stirred for 1 hour at 70°C to disperse uniformly. Finally, a 100 μL of uniformly distributed suspension was coated on the PGE surface using the drop-cast method with the help of a microsyringe [25]. To improve its interface stability and bonding force, the modified electrode was oven-dried at 60°C for 12 hours [26]. Bare PGE (1 cm in length and 0.2 cm in diameter) was prepared by soaking in distilled water for 24 hours and rinsed with 0.2 M phosphate-buffered solution (PBS) [27].

2.4. Characterization Techniques. UV-Vis (Azzota SM-1600 SPECTROPHOTOMETER, USA) was used to observe both the maximum wavelength and the absorption spectrum in the wavelength range of 200 nm-800 nm.

The existence of metal-nonmetal functional groups was monitored using Fourier transform infrared (FTIR) spectra with a PerkinElmer FT-IR BX spectrophotometer in the range of 4000-400 cm^{-1} with samples prepared using KBr pellets.

The structural elucidation was examined with powder X-ray diffraction (XRD-7000, Shimadzu, Japan) with a voltage of 40 kV and a current of 30 mA using a Cu Kα X-ray radiation source (1.5406 Å) in the 2θ range of 10°-80°.

Thermogravimetric-differential thermal analyses (TGA-DTA) were carried out on a DTG-60H detector (Shimadzu, Japan) at a 50 mL min^{-1} sample flow rate.

Differential scanning calorimetry (PerkinElmer, DSC 4000, USA) was carried out at 20 mL min^{-1} and 10°C min^{-1} flow and heating rates, respectively, under nitrogen (N_2) atmosphere.

The surface morphology and elemental composition were investigated using scanning electron microscopy-energy-dispersive X-ray analysis (SEM-EDX, JEOL Ltd. instrument with a model of JCM-6000Plus).

Electrochemical measurements were carried out with a three-electrode electrochemical workstation (Biologic SP-300, Canada) containing bare/modified PGE, Ag/AgCl, and Pt wire as the working, reference, and counter electrodes, respectively. Electrochemical impedance spectroscopy (EIS) was measured in the frequency range of 200 kHz-10 MHz at AC perturbation of 10 mV. The cyclic voltammetry (CV) was also measured in the potential window between -0.8 V and +0.8 V at a scan rate of 50 mV s^{-1}. All the measurements were carried out in 100 mM phosphate-buffered electrolyte solution (pH = 7.4). EC-Lab v10.36 software was used for fitting both the cyclic voltammogram and the EIS spectrum.

2.5. MFC Setup and Operation. To show the bioelectrocatalytic catalytic activities of ternary composites compared with bare PGE, a double-chamber MFC setup was constructed from two equal glass Büchner flasks connected with a glass tube (9 cm in length and 1.1 cm in diameter) which acts as a salt bridge filled with 12 g of KCl and 3 g agar shown in Figure 1. Unmodified PGE and modified PGE with the α-MnO_2/NiO/PANI ternary composite catalyst were used as an anode while bare PGE was used as a cathode. The anode bioreactor was prepared from measurable artificial wastewater containing 160 mg L^{-1} of glucose substrate, 5840 mg L^{-1} of NaCl, 100 mg L^{-1} of KCl, 250 mg L^{-1} of NH_4Cl, 12,000 mg L^{-1} of $Na_2HPO_4 \cdot 12H_2O$, 2570 mg L^{-1} of $NaH_2PO_4 \cdot 2H_2O$, 840

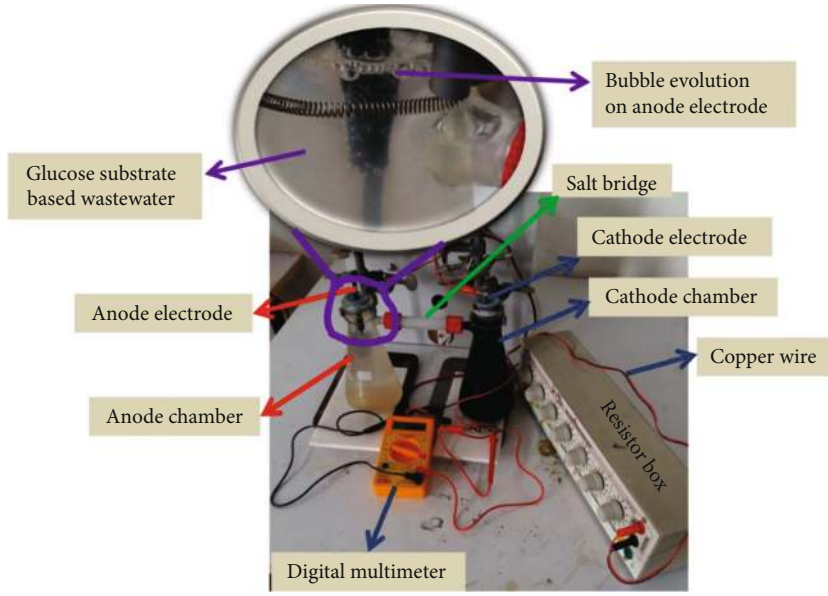

Figure 1: Photograph of double-chambered MFC.

$mg\,L^{-1}$ of $MgCl_2{\cdot}6H_2O$, $500\,mg\,L^{-1}$ of $FeCl_3$, $2\,mg\,L^{-1}$ of $MnSO_4{\cdot}H_2O$, $5\,mg\,L^{-1}$ of $CaCl_2$, and $340\,mg\,L^{-1}$ of yeast extract to fulfill the micronutrient deficiency [28]. The anode was inoculated with *E. coli* cultured from wastewater effluents collected from the Adama Science and Technology University wastewater treatment plant, Adama, Ethiopia (latitude $8^{\circ}33'43.56''$ north and longitude $39^{\circ}17'23.28''$ east), using a sterile glass bottle tied up with a lightweight steel round stick. The anode chamber was kept airtight and filled completely with $160\,mg\,L^{-1}$ of glucose substrate as a carbon source with inoculum added to achieve anaerobic conditions [29]. The cathode chamber was filled with 50 mM $KMnO_4$ which was dissolved in a neutral medium (100 mM, pH 7.40) PBS.

2.6. Power Measurement. The open-circuit voltage (OCV) and closed-circuit voltage (CCV) were monitored for 3 hours/day after 5 minutes of stabilization for every 5-minute continuous interval using a digital multimeter (DT830D, Haoyue, China). The polarization determination was monitored from CCV against external resistors for a 15-minute time interval using the Decade Resistance Box (ANSHUMAN, Model: DRB-7T) by varying an external resistance from 10 kΩ to 200 Ω. The current flow across each resistor was determined by using Ohm's law: $I = V/R$ and $P = IV$, where P is power, I is current, and V is measured voltage. Similarly, the current (J) and power (P) densities were calculated from the ratio of current and power to surface area (A) of the anode, respectively.

2.7. COD Removal and CE Measurement. To measure the chemical oxygen demand (COD) and coulombic efficiency (CE), the following formulas would help to explain degradation efficiency [30]:

$$\mathrm{COD} = \left(\frac{\mathrm{COD_{in}} - \mathrm{COD_{out}}}{\mathrm{COD_{in}}}\right) \times 100\%, \quad (1)$$

where COD_{in} ($mg\,L^{-1}$) is the influent COD and COD_{out} ($mg\,L^{-1}$) is the effluent COD.

The coulombic efficiency (CE) was measured as the ratio between the electrons transferred to the anode from the microorganism to the theoretical one that can be achieved if all organic substrates were digested by the microorganisms to generate electrons. Therefore, the CE can be calculated for batch reactor conditions as follows [30]:

$$\mathrm{CE} = \frac{M\int_0^t I\,dt}{FbV_{\mathrm{an}}\,\Delta\mathrm{COD}_t}, \quad (2)$$

where M is the oxygen molecular weight (32), I is the current, and t is the time at the maximum power density. F is Faraday's constant, $b = 4$ indicates the number of electrons exchanged per mole of oxygen, V_{an} is the anodic solution volume, and ΔCOD is the change in chemical oxygen demand after time t.

3. Results and Discussions

3.1. UV-Vis Analysis. The UV-Vis spectra of α-MnO_2 and PANI as well as α-MnO_2/PANI and α-MnO_2/NiO/PANI nanocomposites are given in Figure 2. In pure α-MnO_2, the absorption peak observed at about 285 nm might be an electronic transition from the O_{2p} valence band to the Mn_{3d} conduction band or from the triply degenerate (t_{2g}) valence band to the doubly degenerate conduction band (e_g) if the shape is purely tetrahedral, as shown in Figure 2(a) [22]. The absorption peak for PANI found at about 267 nm and near 405 nm indicated $\pi \rightarrow \pi^*$ transitions of the benzenoid ring and polaron $\rightarrow \pi^*$ transitions, respectively, as shown in

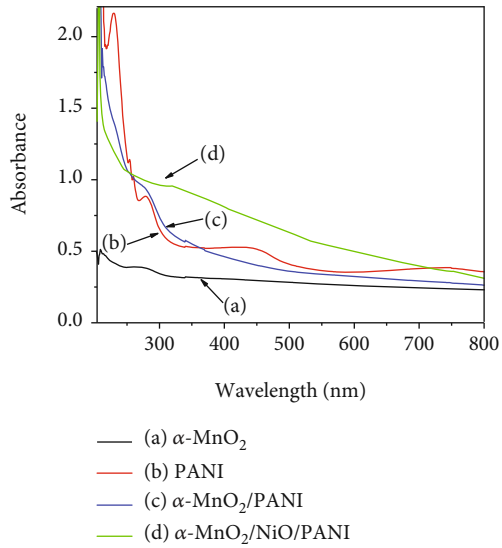

FIGURE 2: UV-Vis absorption spectra of the α-MnO_2 (a), PANI (b), α-MnO_2/PANI nanocomposite (c), and α-MnO_2/NiO/PANI nanocomposite (d).

Figure 2(b) [31]. The shift to a higher wavelength in the α-MnO_2/PANI nanocomposite than pure PANI is attributed to the chemical interactions between α-MnO_2 NPs and the quinoid ring of the PANI backbone (see Figure 2(c)) [13]. In the case of α-MnO_2/NiO/PANI nanocomposites shown in Figure 2(d), a blueshift (below 300 nm) with a maximum absorption peak in the near-visible region (300 nm-400 nm) than pure PANI and α-MnO_2/PANI may indicate the decreasing polaron path during PANI conjugation due to the loading of α-MnO_2/NiO NPs in the conductive PANI matrix. According to Mohammad Shafiee et al. [23], a blue-shift found on the UV region might be a strong interaction between metal oxide d orbitals and π orbitals found in the polymeric material. So, the significant redshift above 300 nm in the α-MnO_2/NiO/PANI nanocomposite supports its improvements in electrical conductivity due to the polaron movement across the extended conjugation [32].

3.2. FTIR Analysis. The FTIR spectra of the pure NPs and their nanocomposites are shown in Figure 3. The spectra shown in Figure 3(a) demonstrated that characteristic peaks found at 3422, 3304, 596, and 495 cm^{-1} are attributed to –OH surface water stretching, H-O-H bending, O-Mn-O stretching collision, and Mn-O bond stretching vibrations, respectively [22]. The bands found at 3448, 2924, 1636, 1445, 1098, and 969 cm^{-1} showed N-H stretching, aromatic C-H stretching, quinoid ring stretching vibration, and benzenoid ring vibrations, respectively, as indicated in Figure 3(b) [33]. The reduction in peak intensity of PANI found in α-MnO_2/PANI and the reduction in peak intensity at about 1098 cm^{-1} and 969 cm^{-1} as well as a new peak appearing at about 508 cm^{-1} with better peak intensity than pure PANI indicate the clear transformation of PANI in the nanocomposite (see Figure 3(c)). Moreover, an intense peak found at about 1094 cm^{-1} and 511 cm^{-1} illustrates the successful NiO

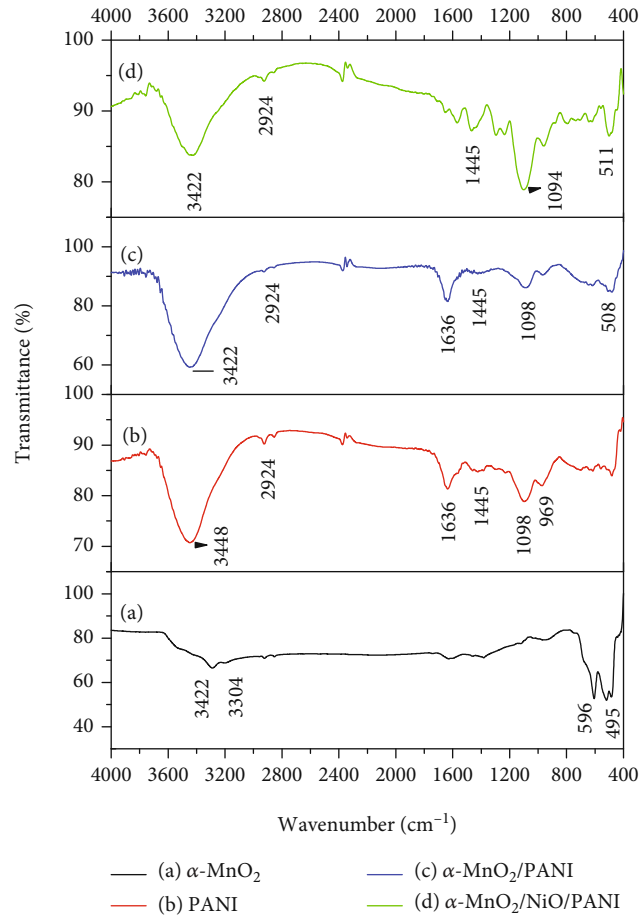

FIGURE 3: FTIR spectra of the α-MnO_2 (a), PANI (b), α-MnO_2/PANI nanocomposite (c), and α-MnO_2/NiO/PANI nanocomposite (d).

interfaced in the MnO_2/PANI binary nanocomposite system, as shown in Figure 3(d).

3.3. XRD Analysis. The XRD patterns of pure α-MnO_2 and PANI as well as α-MnO_2/PANI and α-MnO_2/NiO/PANI nanocomposites are shown in Figure 4. Figure 4(a) describes the spectrum of α-MnO_2 which has three intense characteristics at $2\theta = 12.479°$, 25.228°, and 37.218°, which are attributed to the diffraction planes found at (110), (220), and (211), respectively, which were indexed with the standard XRD pattern of α-MnO_2 (Crystallography Open Database (COD), Entry # 96-151-4117 (space group: I4/m (87))) with pure tetragonal phase and lattice parameters containing $a = 9.78760\,Å$ and $c = 2.86500\,Å$ [22]. The XRD pattern shown in Figure 4(b) showed two broad characteristic peaks found at $2\theta = 20.494°$ and 25.413°, which are indexed to diffraction planes at (100) and (110), respectively, due to the characteristic chain of PANI [34]. For the α-MnO_2/PANI nanocomposite, its diffraction peaks are almost similar to those of pure PANI in all planes except changes that occurred at $2\theta = 21.151°$ indexed at (100) (Figure 4(c)). The better peak symmetry on α-MnO_2/PANI than pure PANI showed that the presence of α-MnO_2 NPs results in its crystal structure distortion during the polymerization reaction. The spectrum of the α-MnO_2/NiO/PANI nanocomposite is similar to that

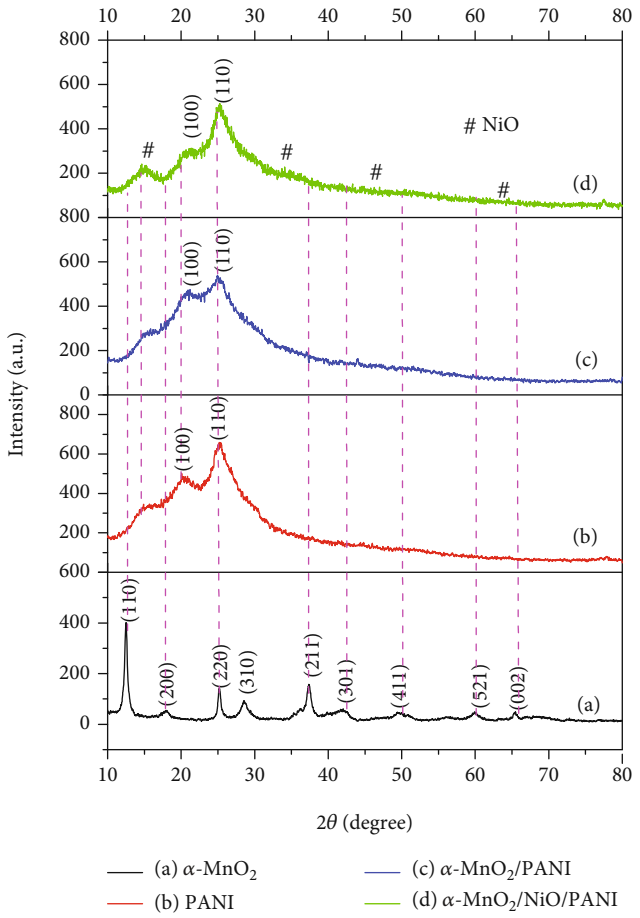

FIGURE 4: XRD patterns of the α-MnO_2 (a), PANI (b), α-MnO_2/PANI nanocomposite (c), and α-MnO_2/NiO/PANI nanocomposite (d).

of the α-MnO_2/PANI nanocomposite, as shown in Figure 4(d). The peak at $2\theta = 21.151^\circ$ and 25.413° may be attributed to the interaction of α-MnO_2 insertion in PANI while the intense broad peak at 14.208° and 25.684° indexed at (101) and (110) planes is due to the incorporation of NiO NPs in the conductive PANI matrix. The proof was identified and indexed from the standard XRD pattern of NiO (COD, Entry # 96-432-9324 from Match! 3 phase identification software) and in good agreement with the literature [35]. The overall crystallite size and d-spacing are summarized in Table 1.

3.4. Thermal Analysis. The thermal stability of pure α-MnO_2 and PANI nanomaterials as well as α-MnO_2/PANI and α-MnO_2/NiO/PANI nanocomposites was examined. Figure 5(a) (i) shows that at the temperature of 146.13°C, the weight loss amounted to be -5.024%, which can be reasonably attributed to existing water removal from the surface and lattice of the nanostructure, while the weight loss of -8.381% found at a temperature of 888.16°C might be the phase transformation of α-MnO_2 to Mn_2O_3 [36]. In Figure 5(a) (ii–iv), PANI, α-MnO_2/PANI, and α-MnO_2/NiO/PANI materials followed a similar weight loss pattern in the four major stages of weight loss. The first two stages of weight loss up to 150°C were attributed to the loss of volatile impurities and surface adsorbed water. The weight loss from 150°C to 500°C might be assigned to the removal of higher oligomers and other remaining residuals [37]. The presence of subsequent weight loss found on the PANI and nanocomposites is due to the thermooxidative decomposition of the PANI chain in the temperature range of 500°C-915°C [37].

The DTA curve shown in Figure 5(b) (i) revealed that α-MnO_2 has two endothermic peaks with more stability property, but the curve shown in Figure 5(b) (ii) attributed to the exothermic decomposition of PANI at a temperature of 210.46°C and 524.31°C is due to the different oxidation products [38]. Finally, the DTA curves shown in Figure 5(b) (iii and iv) that peak at 503.44°C and 467.70°C are for α-MnO_2/-PANI and α-MnO_2/NiO/PANI, respectively. This revealed that α-MnO_2 and α-MnO_2/NiO have a clear interaction with PANI and increase stabilization. The lower temperature peak existence on both composites than pure PANI is due to the fast loss of different products from the polymer decomposition [39]. The summarized weight loss and peak analysis steps are given in Tables 2 and 3.

Figure 5(c) illustrates the typical DSC thermogram for the prepared materials. As shown in Figure 5(c) (i), the endothermic temperature found at 181.13°C justified the glass transition (T_g) of α-MnO_2 NPs during thermal decomposition to Mn_2O_3 under N_2 atmosphere [22]. The broad endothermic transition temperature at about 116.37°C for PANI is attributed to the bounded water loss, as shown in Figure 5(c) (ii). The fall of broad endothermic peaks on pure α-MnO_2 and PANI components showed the clear integration of α-MnO_2 and α-MnO_2/NiO in the conductive PANI matrix to form new and stable nanocomposite formations shown in Figure 5(c) (iii and iv).

3.5. SEM-EDX Analysis. Figure 6(a) shows the SEM micrographs of the as-prepared α-MnO_2 nanoparticles with ball-shaped flower-like architecture. Figure 6(b) shows the non-uniform, rough, and closely packed irregular granular micrographs for pure PANI. The clear distribution of α-MnO_2 nanoparticles over granular PANI is shown in Figure 6(c). The surface modification and binary composite formations clearly contribute to the better surface size distribution image of α-MnO_2/NiO/PANI (Figure 6(d)). The incorporation of MnO_2 and NiO nanoparticles has changed the granular structure of PANI into a more ball-like spherical structure. The elemental composition of this ternary composite contains Mn, Ni, C, O, and codopant elements (S and Cl) with K traces (see Figure 6(e)). The excess of chlorine resulted from its adsorption on the surface of the salt or was trapped in this salt as anilinium chloride (emeraldine salt) during the reaction procedure [40]. The presence of sulfur which originated from APS on the synthesized material improves the electrocatalytic activity on the bare anode [41]. It is noted that the detection of elements using EDX is below 0.01 wt% [42]. So, in this investigation, the element nitrogen is not detected on the spectrum. At low energy resolution, peak overlap may occur between the nitrogen and the polyaniline carbon signal. To prevent this, some researchers have used a high-energy resolution instrument [43].

Table 1: XRD data used for calculating the interlayer spacing and crystallite size of different samples.

Sample type	d-spacing (nm)	2θ (degree)	FWHM (degree)	Miller indices (hkl)	Crystallite size (nm)
α-MnO_2	0.69792	12.479	0.3875	1 1 0	21.55
	0.35008	25.228	0.4050	2 2 0	21.00
	0.23830	37.218	0.4453	2 1 1	19.67
					Average = 20.74
PANI	0.43275	20.494	2.245	1 0 0	3.56
	0.38851	25.413	10.024	1 1 0	0.79
					Average = 2.18
α-MnO_2/PANI	0.41971	21.151	1.545	1 0 0	12.48
	0.35021	25.413	14.831	1 1 0	0.54
					Average = 6.51
α-MnO_2/NiO/PANI	0.62286	14.208	2.835	1 0 1	2.95
	0.34657	25.684	11.775	1 1 0	0.72
					Average = 1.84

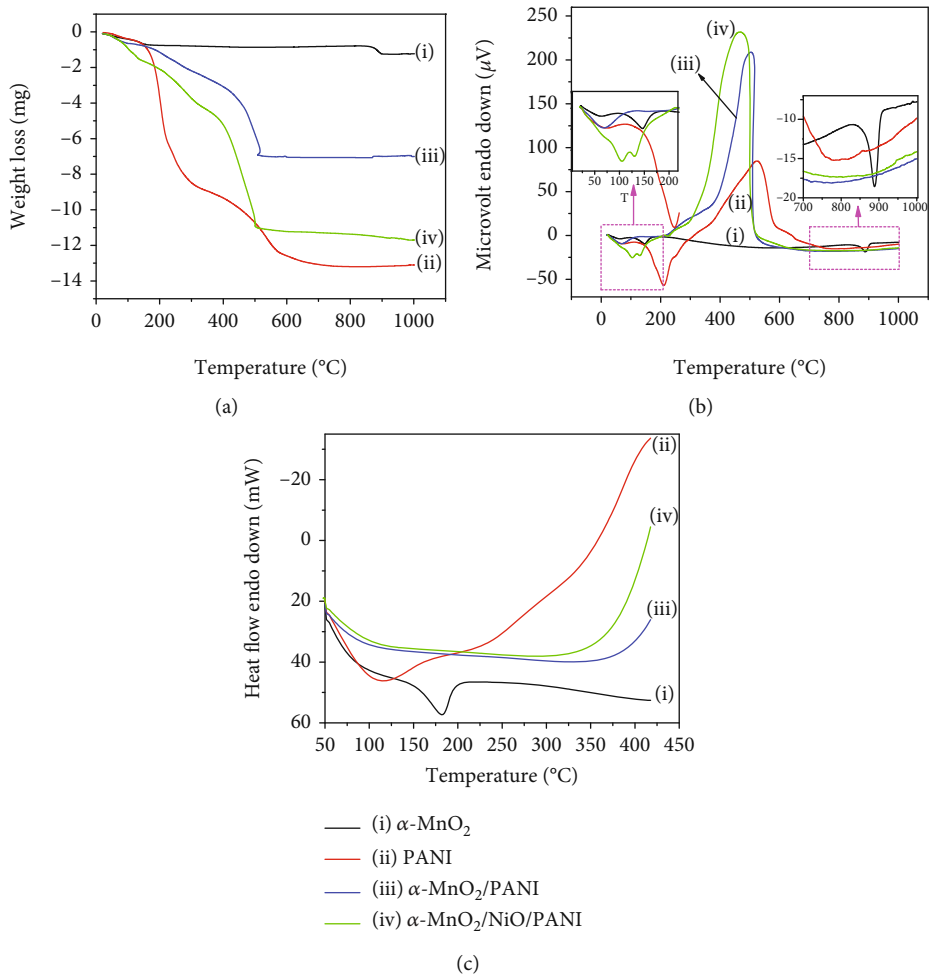

Figure 5: Thermal properties of α-MnO_2, PANI, α-MnO_2/PANI, and α-MnO_2/NiO/PANI samples: TGA (a), DTA (b), and DSC (c) profiles.

3.6. Surface Roughness. Nanomaterial surface roughness physical performance analyses have a significant impact on various electrochemical applications [44]. Hence, the surface topography loaded from SEM images of α-MnO_2, PANI, and their nanocomposites was analyzed using Gwyddion software, as shown in Figure 7. The degree of surface roughness that arises from its parameters quantifies the direct pore occurrence from 2D (Figure 7(a1, b1, c1, and d1)) and 3D

Table 2: Onset degradation temperature and corresponding weight loss.

Weight loss analysis	α-MnO_2		PANI				α-MnO_2/PANI				α-MnO_2/NiO/PANI			
Step	1st	2nd	1st	2nd	3rd	4th	1st	2nd	3rd	4th	1st	2nd	3rd	4th
Temperature (°C)	146.13	888.16	37.67	205.62	319.78	692.81	19.63	225.68	493.75	509.59	84.70	198.49	473.42	914.35
TGA (mg)	-0.660	-1.101	-0.072	-4.393	-8.732	-13.057	-0.044	-1.433	-5.440	-6.917	-0.644	-2.088	-8.855	-11.589
TGA (%)	-5.024	-8.381	-0.520	-31.721	-63.051	-94.281	-0.525	-17.092	-64.885	-82.502	-4.460	-14.459	-61.318	-80.251

TGA = thermogravimetric analysis.

Table 3: Differential thermal analysis (DTA) results.

DTA peak analysis	α-MnO_2		PANI		α-MnO_2/PANI		α-MnO_2/NiO/PANI	
Step	1st	2nd	1st	2nd	1st	2nd	1st	2nd
Temperature (°C)	146.13	888.16	210.46	524.31	68.25	503.44	105.12	467.70
DTA (μV)	-9.68	-18.57	-56.90	84.79	-9.36	208.79	-25.30	231.86

(Figure 7(a2, b2, c2, and d2)) maps. These quantified parameters are mean roughness (R_a), mean square roughness (R_q), surface skewness (R_{sk}), and kurtosis coefficient (R_{ku}) [45]. So, from this study, all representative parameters were examined by the row statistical analysis approach shown in Table 4. The R_a value of the α-MnO_2/NiO/PANI nanocomposite was 23.65 ± 5.652 nm. This value was higher than α-MnO_2 and PANI, and even the α-MnO_2/PANI nanocomposite has a lower$R_a$value. This shows that α-MnO_2/NiO/PANI has a better rough surface than others which is a clear indication for its best surface area and reactive surface site [46]. The same principle is also proved from its R_q (28.55 ± 5.617 nm) values, indicating the degree of surface roughness variation is much higher than others. The R_{sk} of α-MnO_2/NiO/PANI nanocomposites shows a higher positive value than other prepared materials. The higher positive value indicated that there are more troughs (regions of positive curvature) than peaks on the surface. The R_{ku} value of the α-MnO_2/NiO/-PANI nanocomposite was -0.7148 ± 0.566. The results show that the pore size distribution of the α-MnO_2/NiO/PANI nanocomposite is more scattered (i.e., the pore size distribution is not compact or more concentrated) than other nanomaterials. Therefore, from all parametric information, we conclude that α-MnO_2 and NiO nanomaterials are successfully incorporated in the conductive PANI matrix. Such dispersion enhances the mechanical properties [47] and thermal stability of the nanocomposites which was supported by the thermal analysis. Not only these, the addition of the above metal oxides on the polymer matrix led to increased surface roughness and increased multifunctionality by forming hierarchical shapes of the materials [48]. For comparison, all parameters are given in Table 4.

3.7. Electrochemical Property. In order to evaluate the electrochemical performances of unmodified and modified electrodes, CVs were performed under phosphate-buffered electrolyte solution, as shown in Figure 8. A pair of quasi-reversible redox peaks was dominated on the nanocomposite-modified electrode from the best fit line of I_p versus $v^{1/2}$. The reversibility of these peaks suggests that the fabricated nanocomposite does not decompose during the charge transfer mechanism, and this helps for fast electron transfer ability. A pair of weak redox peaks was observed at bare PGE with anodic (I_{pa}) and cathodic peak current (I_{pc}) values of 0.735 mA and 4.379 mA, respectively, which was lower than other electrodes, as shown in Figure 8(a). After modification, the peak current observed by PGE was 2.685 mA and 6.079 mA for I_{pa} and I_{pc}, respectively. The bare electrode modified by the α-MnO_2/NiO/PANI nanocomposite was increased by 3-fold anodic peak current than unmodified PGE. The rest of the peak currents determined by α-MnO_2, PANI, and α-MnO_2/PANI-modified PGE are given in Table 5. The increase in peak current in all modified electrodes indicated the better electrocatalytic activity of α-MnO_2 NP interaction in the PANI matrix and good attribution of the nanocomposite on the PGE surface. So, the anodic peak current was found to be higher in α-MnO_2/NiO/PANI/PGE (2.685 mA at a potential of -0.573 V) than the other modified electrodes including bare PGE. This suggests that dispersion of α-MnO_2/NiO bimetallics in the PANI matrix modified the surface activity of PGE and changes its anodic peak potential. This activity extends to increase the total charge storing performance in the order of α-MnO_2/NiO/-PANI/PGE>α-MnO_2/PANI/PGE>PANI/PGE>α-MnO_2/PGE>PGE anode electrode, as shown in Figure 8(b). This order facilitates a conductive anode formation. It indicated that α-MnO_2/NiO/PANI/PGE exhibited a fast electron transfer rate that enables to increase electrical conductivity due to having lower peak-to-peak potential separation ($\Delta E_p = 0.216$ V) than other electrodes. The effective surface area (effective electroactive area) of the electrode is the main factor which affects the electrocatalytic performance activities. So, to determine this area, the equation proposed by Randles-Sevčik was followed [7]:

$$I_{pa} = \left(2.69 \times 10^5\right) n^{3/2} D^{1/2} v^{1/2} AC, \quad (3)$$

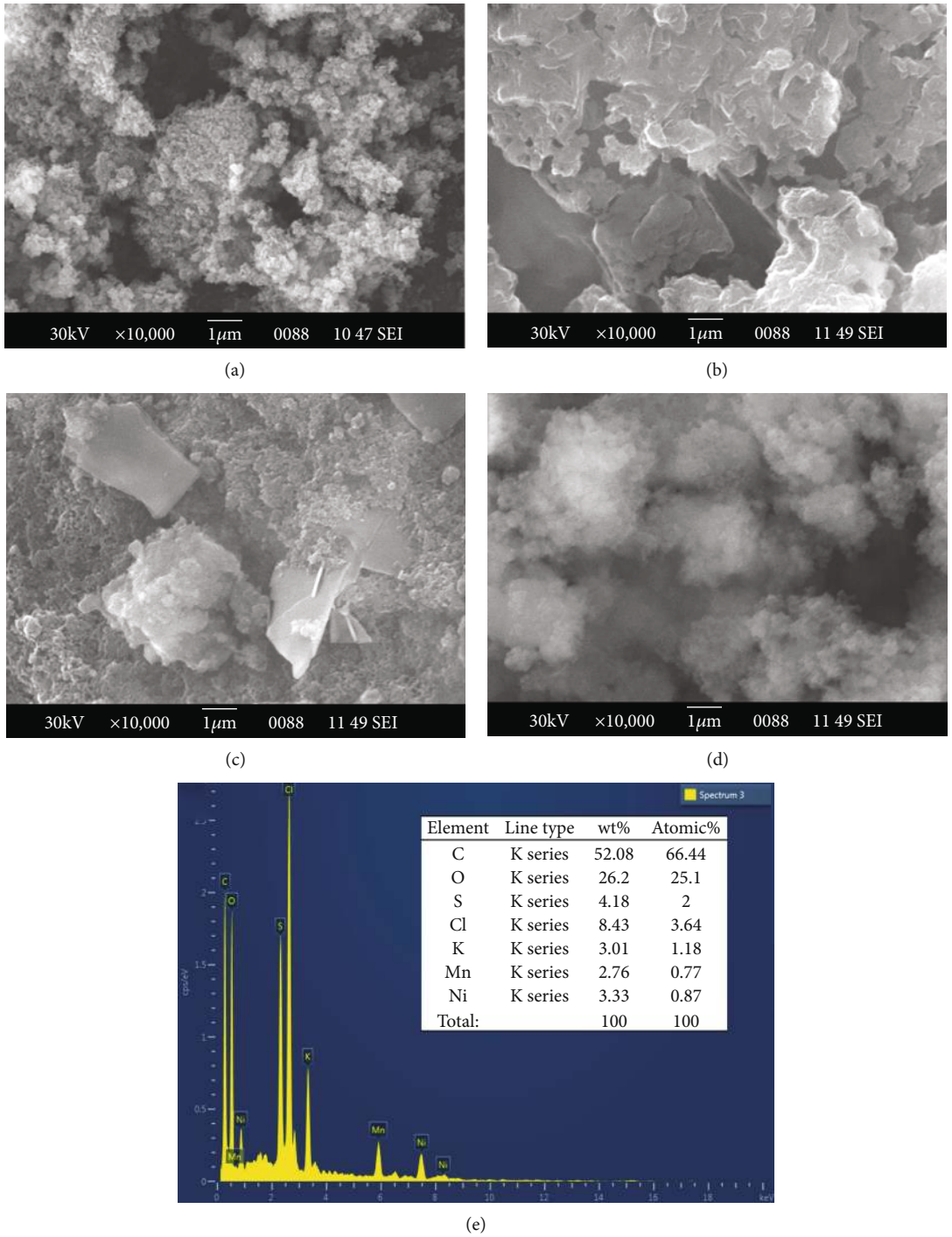

Figure 6: SEM topographies of (a) α-MnO_2, (b) PANI, (c) α-MnO_2/PANI, and (d) α-MnO_2/NiO/PANI and (e) EDX spectrum of α-MnO_2/NiO/PANI.

where I_{pa} is the anodic peak current (A), n is the number of electron transfer, D is the diffusion coefficient of HPO_4^{2-} (7.60×10^{-6} cm^2/s [49]), v is the scanning rate ($V\,s^{-1}$), A is the effective electroactive area (m^2), and C is concentration of PBS ($mol\,cm^{-3}$). Their effective areas were described to be 0.00269, 0.00695, 0.00945, 0.00942, and 0.00984 cm^2 for unmodified PGE, α-MnO_2/PGE, PANI/PGE, α-MnO_2/PANI/PGE, and α-MnO_2/NiO/PANI/PGE, respectively. These results suggest that α-MnO_2/NiO/PANI nanocomposite-modified PGE has the largest effective surface area which helps to facilitate a fast electrocatalytic activity as observed from its high peak current.

To visualize the possible redox reactions found at the electrode, dissolved oxygen PBS interfaces are as follows [50]:

$$M(s) + HPO_4^{2-}(aq) \rightleftarrows M_3PO_4(s) + H^+(aq) + 3e^- \quad (4)$$

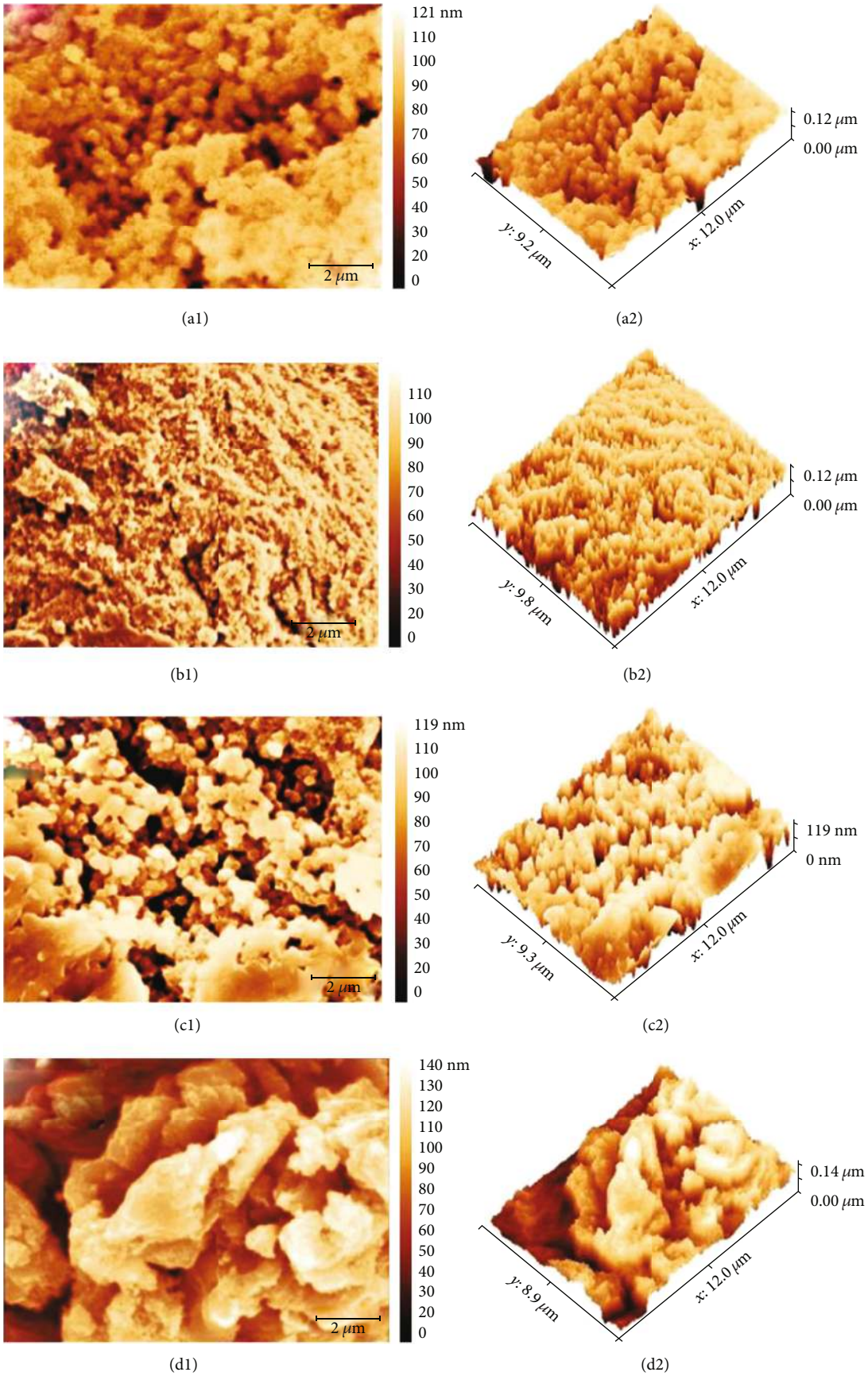

Figure 7: 2D and 3D SEM images of α-MnO_2 (a1, a2), PANI (b1, b2), α-MnO_2/PANI (c1, c2), and α-MnO_2/NiO/PANI (d1, d2).

Table 4: Surface roughness row statistical quantity results for different samples acquired from SEM entire image analysis.

Catalyst	R_a (nm)	R_q (nm)	R_{sk}	R_{ku}
α-MnO_2	13.11 ± 3.163	17.21 ± 3.587	−0.8903 ± 0.5439	0.9627 ± 1.798
PANI	19.96 ± 2.264	24.22 ± 2.423	−0.3789 ± 0.1872	−0.5079 ± 0.342
α-MnO_2/PANI	22.92 ± 3.648	28.15 ± 3.645	−0.6072 ± 0.3500	−0.2429 ± 0.709
α-MnO_2/NiO/PANI	23.65 ± 5.652	28.55 ± 5.617	−0.2178 ± 0.4192	−0.7148 ± 0.566

Note: R_a: mean roughness; R_q: mean square roughness (RMS); R_{sk}: surface skewness; R_{ku}: kurtosis coefficient.

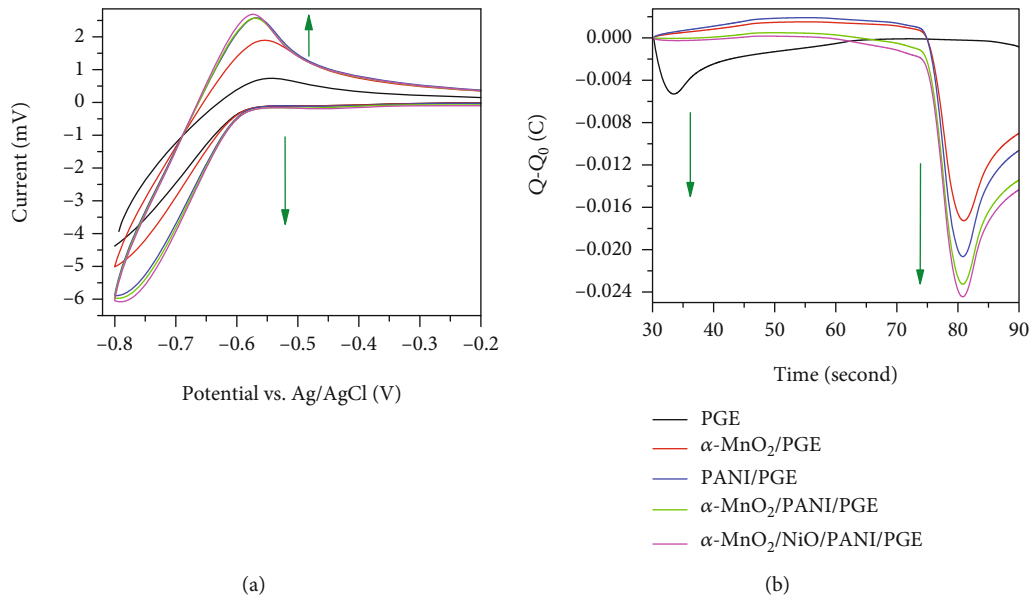

Figure 8: Cyclic voltammogram (a) and total charge exchanged $Q - Q_0$ (b) of bare PGE (black line), α-MnO_2/PGE (red line), PANI/PGE (blue line), α-MnO_2/PANI/PGE (green line), and α-MnO_2/NiO/PANI/PGE (pink line) electrodes in 100 mM PBS (pH = 7.4) at a scan rate of 50 mV s^{-1}.

Table 5: Summary of the redox current and potential peak formed on the prepared anode electrodes.

Electrode	PGE	α-MnO_2/PGE	PANI/PGE	α-MnO_2/PANI/PGE	α-MnO_2/NiO/PANI/PGE
I_{pa} (mA)	0.735	1.897	2.579	2.569	2.685
I_{pc} (mA)	4.379	5.015	5.895	5.975	6.079
$I_{p,av}$ (mA)	2.557	3.456	4.237	4.272	4.382
E_{pa} (V) vs. Ag/AgCl	-0.543	-0.553	-0.568	-0.570	-0.573
E_{pc} (V) vs. Ag/AgCl	-0.800	-0.799	-0.798	-0.794	-0.789
$\Delta E_p = E_{pa} - E_{pc}$ (V) vs. Ag/AgCl	0.257	0.246	0.230	0.224	0.216
$(Q\text{-}Q_0)_{average}$ (mC)	5.291	17.267	20.659	23.258	24.456

Average peak current $(I_{p,av}) = (I_{pa} + I_{pc})/2$.

where M stands for catalysts such as PGE, α-MnO_2, PANI, α-MnO_2/PANI, and α-MnO_2/NiO/PANI.

As observed from the CV result, α-MnO_2/NiO/PANI nanocomposite-modified PGE was the best electrode among the rest. Therefore, the effect of the scan rate on the cyclic voltammetric performance of α-MnO_2/NiO/PANI/PGE is shown in Figure 9(a) at the scan rates (5-200 m Vs^{-1}). The responses of both I_{pa} and I_{pc} currents gradually increase with increasing scan rates along with oxidation and reduction peak potentials that shift to the right and left, respectively. Figure 9(b) justifies the linear dependence of both I_{pa} and I_{pc} versus the square root of the scan rate with linear regression equations of $I_{pa} = 0.30405v^{1/2} + 0.29912$ ($R^2 = 0.97$) and $I_{pc} = -0.63452v^{1/2} - 1.1702$ ($R^2 = 0.98$). The dependence of peak potentials (E_{pa} and E_{pc}) against the scan rate is also shown in Figure 9(c). Hence, we imply that the nature of the redox process occurring on the electrode surface is nearly

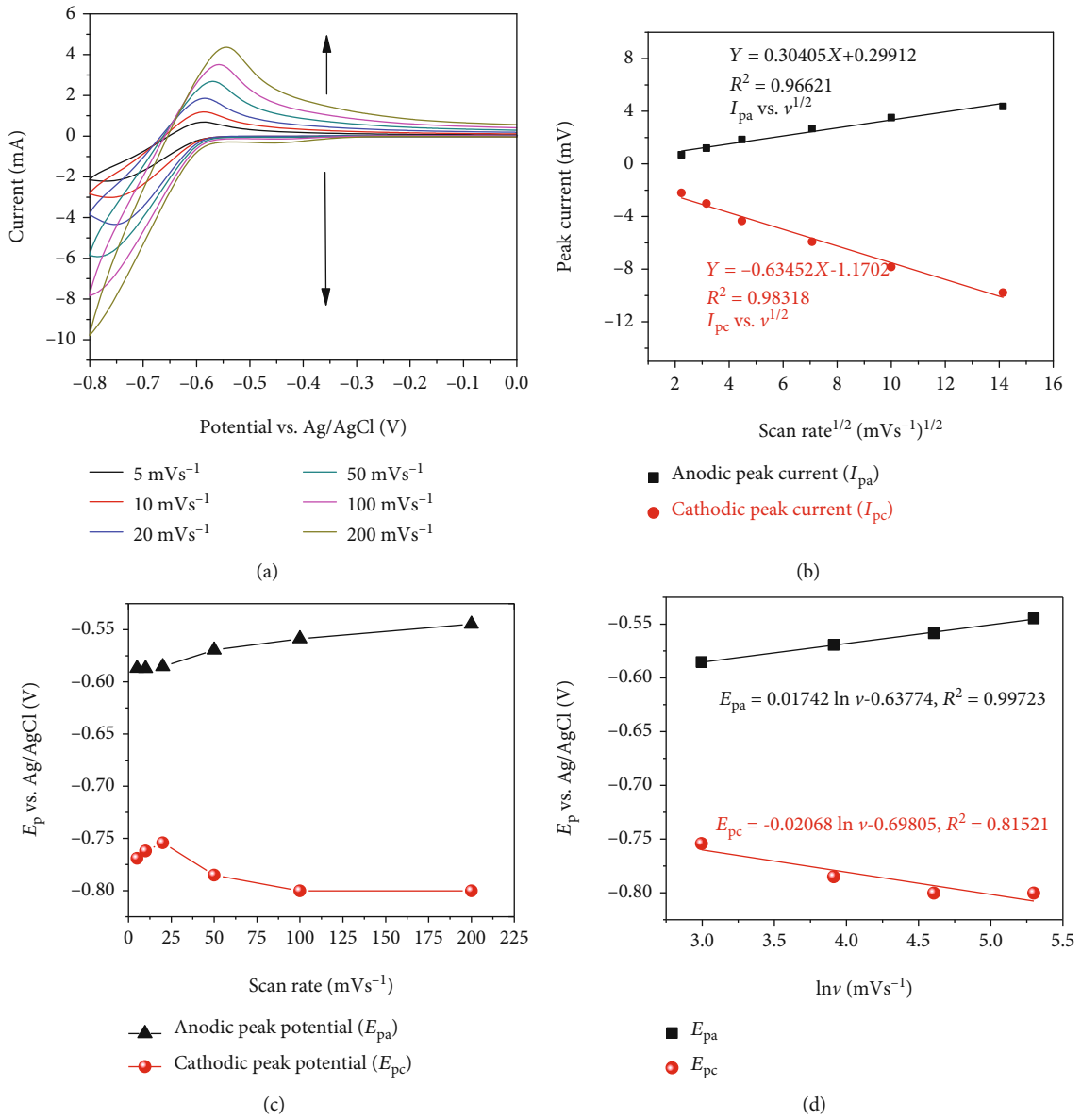

FIGURE 9: Cyclic voltammograms of α-MnO_2/NiO/PANI/PGE in pH 7.4 PBS at different scan rates (a), linear plots of peak currents versus the square root of the scan rate ($v^{1/2}$) (b), linear plots of peak potential versus scan rates (c), and linear plots of peak potential versus the natural logarithm of the scan rate (ln v) (d).

reversible (quasi-reversible) [20] and is clearly a diffusion-controlled process [51]. The anodic peak potential (E_{pa}) was highly correlated with the natural logarithm of the scan rate (ln v) for α-MnO_2/NiO/PANI/PGE in PBS (pH = 7.4) (Figure 9(d)). To evaluate the electrochemical parameters from such linearity, the Laviron equation was applied as follows [52]:

$$E_{pa} = E^o + \frac{RT}{(1-\alpha)nF} + \frac{RT}{(1-\alpha)nF} \ln v, \quad (5)$$

where E^o is the formal potential ($E_{pa} + E_{pc}/2$), α is the charge transfer coefficient of the system, v is the scan rate, n is the number of electron transfer, R is the universal gas constant (8.314 J mol^{-1} K^{-1}), T = 298 K, F = 96,493 C mol^{-1}, and k_s is the heterogeneous electron transfer rate constant. From the slope of E_{pa} vs. ln v, α = 0.51. So, if α is closer to 0.5, the electrode reaction is quasi-reversible and governed by the diffusion-controlled process [53].

The Laviron equation [54] was applied to calculate k_s for each electrode as well as electron transfer at each scan rate:

$$\log k_s = \alpha \log (1-\alpha) + (1-\alpha) \log \alpha - \log \frac{RT}{nFv} - \frac{\alpha(1-\alpha)nF}{2.3RT} \Delta E_p. \quad (6)$$

The calculated k_s value of α-MnO_2/NiO/PANI/PGE at constant scan rates of 50 mV s^{-1} was higher than the rest of

Table 6: Summary of the heterogeneous electron transfer rate constant for different anode electrodes at 50 mV s^{-1}.

Electrode	PGE	α-MnO_2/PGE	PANI/PGE	α-MnO_2/PANI/PGE	α-MnO_2/NiO/PANI/PGE
$\Delta E_p = E_{pa} - E_{pc}$ (V) vs. Ag/AgCl	0.257	0.246	0.230	0.224	0.216
k_s (s^{-1})	2.91776971	2.917832732	2.917924402	2.91795878	2.918004616

Table 7: A heterogeneous electron transfer rate constant for α-MnO_2/NiO/PANI/PGE at different scan rates.

Scan rate (m V s^{-1})	5	10	20	50	100	200
$\Delta E_p = E_{pa} - E_{pc}$ (V) vs. Ag/AgCl	0.182	0.175	0.169	0.216	0.242	0.256
k_s (s^{-1})	0.292	0.584	1.167	2.918	5.836	11.671

the electrode, and this indicated that the α-MnO_2/NiO/PANI nanocomposite is a good facilitator for direct electron transfer between electroactive species and bare PGE (see Table 6). The direct dependence of k_s over peak potential is also given in Table 7.

EIS is an efficient technique to estimate electron transfer properties between electrode surfaces and electrolyte interfaces during redox reactions [52]. The Nyquist plot shown in Figure 10(a) describes that both the α-MnO_2/PANI and α-MnO_2/NiO/PANI composite-modified electrodes have lower solution and charge transfer resistances (R_s and R_{ct}) in the high-frequency regions due to their electrical conductivity improvement. The R_s was determined from a higher frequency intercept on the real axis. The value was in the range of 8.86-9.26 Ω for α-MnO_2/PANI and α-MnO_2/NiO/-PANI composite-modified electrodes. The R_{ct} values of the α-MnO_2/NiO/PANI-modified PGE (788.9 Ω) and α-MnO_2/-PANI/PGE (958 Ω) were lower than that of unmodified PGE (1519 Ω), indicating that the modified anode surface had improved its electrocatalytic activity and surface roughness modification which is responsible for conductive biofilm attachment and EAM growth. The same behavior is also observed from bode plots of frequency-dependent impedance magnitude ($\log|Z|$) (Figure 10(b)). Their diffusion resistance (Z_w) found in the lower frequency region is also lower than pure α-MnO_2 and PANI-modified PGE (see Table 8). The lower diffusion resistance found on the composite-modified PGE showed that the electrode could have a capacitive characteristic due to the finding of phase angles found in the range between -45° and -90° with frequency lower than 100 Hz, as shown in Table 8 and Figure 10(c). Since the capacitive behavior is governed for all electrodes in this phase angle range, and this also suggests their good redox behavior. In the frequency range of 100 Hz-104 Hz, the phase angles decrease rapidly and are close to zero, indicating less electrolyte ion adsorption on electrode surfaces, and resistive behavior is dominated [55]. From this, it is evidenced that the current generation signal in the given time is much better than bare PGE (Figure 10(d)). In Figure 10(e), as the number of cycles increases, the stable current production by α-MnO_2/NiO/PANI ternary composite-modified PGE becomes higher in efficiency than that by α-MnO_2/PANI binary composite-modified PGE due to the long life cycle, high metallic conductivity, and fast charge/-discharge mechanism nature of NiO NMs [56].

3.8. MFC Application. At steady-state conditions, the catalytic activity investigations of composite-modified electrodes under steady-state conditions are shown in Figure 11. The highest open-circuit voltage (OCV) elucidated by α-MnO_2/-NiO/PANI/PGE was 616.72 ± 56.65 mV which was higher than bare PGE with values of 222.36 ± 8.16 mV. A total of 180-minute measurements per day were operated for each electrode (Figure 11(a)). On the second day, the 3-hour measurement was the better time to perform MFC using α-MnO_2/NiO/PANI/PGE than unmodified PGE. From these continuous operations, the higher OCV determination throughout the day using α-MnO_2/NiO/PANI ternary composite-modified PGE was due to the effective adhesion between the *E. coli* colony and the α-MnO_2/NiO/PANI catalyst (Figure 11(b)); these may also be attributed to high charge density capacity after forming the bioanode. These interactions cause increasing conductive biofilm formation by increasing its active surface area on the electrode surfaces which leads to improved fast electron transfer rates on the anode surface in the MFC operation. Each day, OCV values produced by two electrodes are given in Table 9. So, the prepared ternary composite is considered an effective catalyst to increase MFC performances under steady-state conditions.

At non-steady-state conditions, the electrocatalytic activity of α-MnO_2/NiO/PANI composite-modified PGE and unmodified PGE MFC performance tests is given in Figure 12(a). The mean maximum power density of 506.96 mW m^{-2} was delivered with α-MnO_2/NiO/PANI composite-modified PGE while 65.74 mW m^{-2} was obtained using bare PGE. The current density formed at this maximum power density was 2710.51 and 436.52 mA m^{-2} for α-MnO_2/NiO/PANI/PGE and PGE, respectively. The capacity of composite-modified electrodes was 7.71 and 6.21 times higher in power and current densities than that of unmodified PGE. The calculated internal resistance obtained from slopes of measured voltage versus current density [57] was 1183.29 Ω and 3745.74 Ω for α-MnO_2/NiO/PANI/PGE ($R^2 = 0.97916$) and PGE ($R^2 = 0.98858$), respectively. An increase in surface areas lowers the internal resistance found on the modified electrodes, indicating fast extracellular electron transfer between the *E. coli* and the bioanode. The good electron transfer between π orbitals of PANI and d orbitals of Mn^{4+}-Ni^{2+} enables the α-MnO_2/NiO/PANI composite to be effective in power density during glucose oxidation in the given time of operations (Figure 12(b)). Thus, the charge

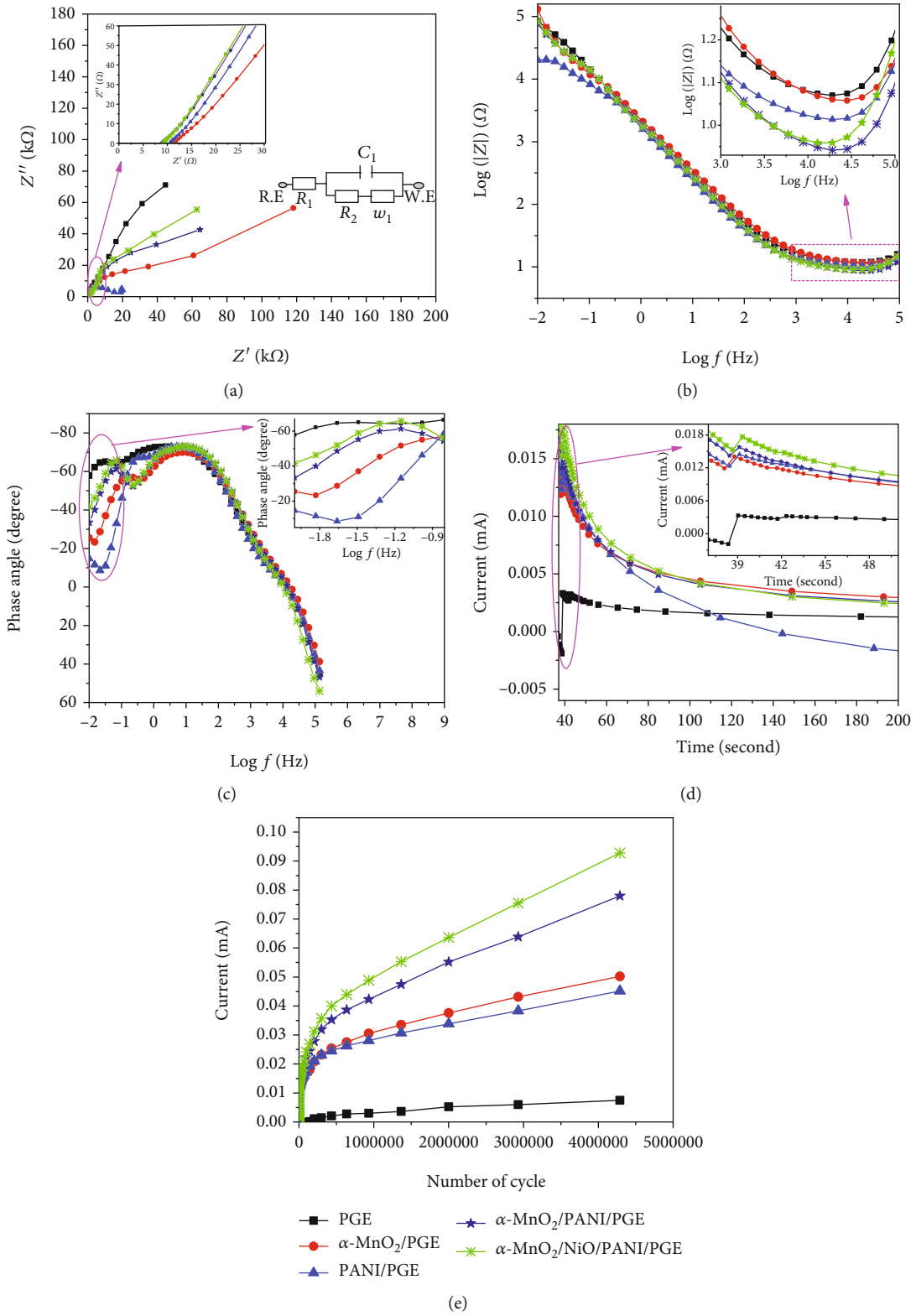

FIGURE 10: Nyquist plot (a) (inset represents the equivalent circuit model after impedance fitting), bode-magnitude (b), bode-phase angle (c), current vs. time (d), and current vs. number of cycles (e) for bare PGE, PANI/PGE, α-MnO_2/PGE, α-MnO_2/PANI/PGE, and α-MnO_2/NiO/PANI/PGE.

Table 8: Electrochemical parameters of the bare PGE, α-MnO_2/PGE, PANI/PGE, α-MnO_2/PANI/PGE, and α-MnO_2/NiO/PANI/PGE electrodes in 100 mM PBS (pH = 7.4) supporting electrolytes.

Electrode	R_1 (R_s) (Ω)	R_2 (R_{ct}) (Ω)	C_2 (C_{dl}) (F)	W_2 (Z_w) (Ω $s^{-1/2}$)	log Z (Ω)	θ (deg)	f (kHz)
PGE	11.91	1519	5.12×10^{-5}	25,283	1.07	-72.851	19.15
α-MnO_2/PGE	11.54	1119	7.42×10^{-5}	13,283	1.06	-70.039	28.32
PANI/PGE	10.47	1071	8.50×10^{-5}	736.1	1.01	-72.854	19.15
α-MnO_2/PANI/PGE	8.86	958	8.01×10^{-4}	448.5	0.94	-73.182	19.15
α-MnO_2/NiO/PANI/PGE	9.26	788.9	9.26×10^{-5}	12,000	0.96	-73.048	19.15

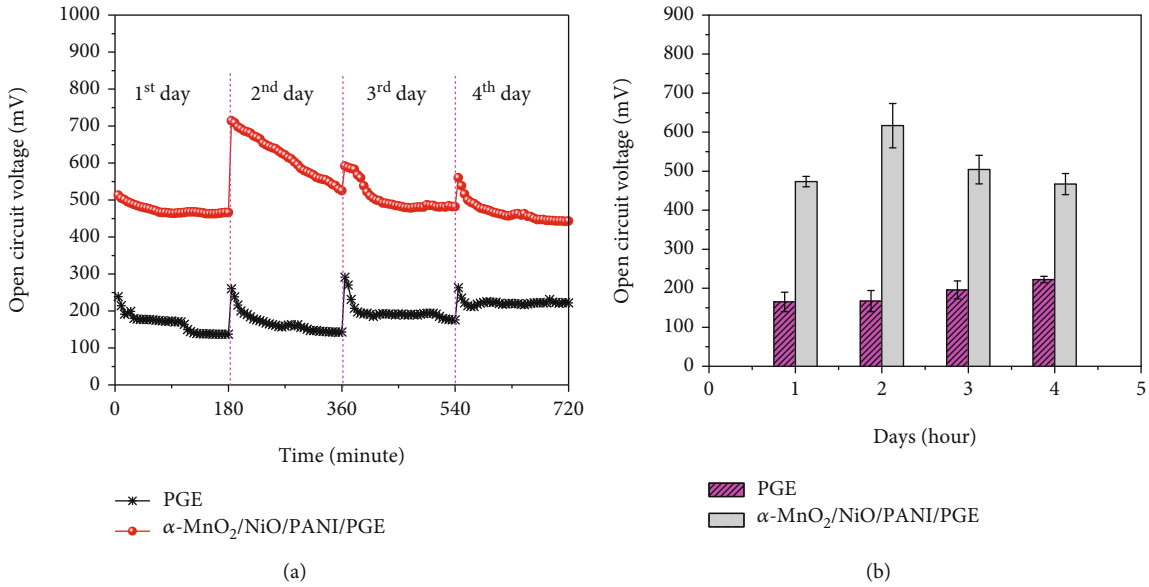

Figure 11: Open-circuit voltage (a) and average open-circuit voltage (b) as a function of time for unmodified PGE and α-MnO_2/NiO/PANI/PGE.

Table 9: OCV output obtained using bare PGE and α-MnO_2/NiO/PANI-modified PGE anode materials.

Time of operation	Electrode	Mean ± SD (mV)	Minimum (mV)	Maximum (mV)
1st day	PGE	164.98 ± 24.84	137	239
	α-MnO_2/NiO/PANI/PGE	473.39 ± 13.29	463	513
2nd day	PGE	166.92 ± 27.03	142	260
	α-MnO_2/NiO/PANI/PGE	616.72 ± 56.65	525	714
3rd day	PGE	195.83 ± 22.92	176	291
	α-MnO_2/NiO/PANI/PGE	504.25 ± 36.61	478	592
4th day	PGE	222.36 ± 8.16	212	263
	α-MnO_2/NiO/PANI/PGE	466.92 ± 27.03	442	560

storage capacity from current discharge as a function of time in the given areas of electrodes was much higher in modified electrodes than bare PGE (see Figure 12(c)). The flow of free charge hindered using bare PGE might arise due to its highest internal resistance found from the polarization curve. This proved that the higher electrical conductivity elucidated from electrochemical performance analysis showed that α-MnO_2/NiO/PANI/PGE produces a higher power output at a lower external load (Figure 12(d)). Hence, the area under time-dependent current at higher external resistance becomes too low due to the continuous charge loss from glucose decomposition. Therefore, the good integration between bimetallic oxides with conductive PANI enhances MFC performance.

3.9. Bioanode Morphology Analysis. The surface morphology of the anode surface is shown in Figure 13. Before MFC operation, an irregular (with flakes in shape) rough surface

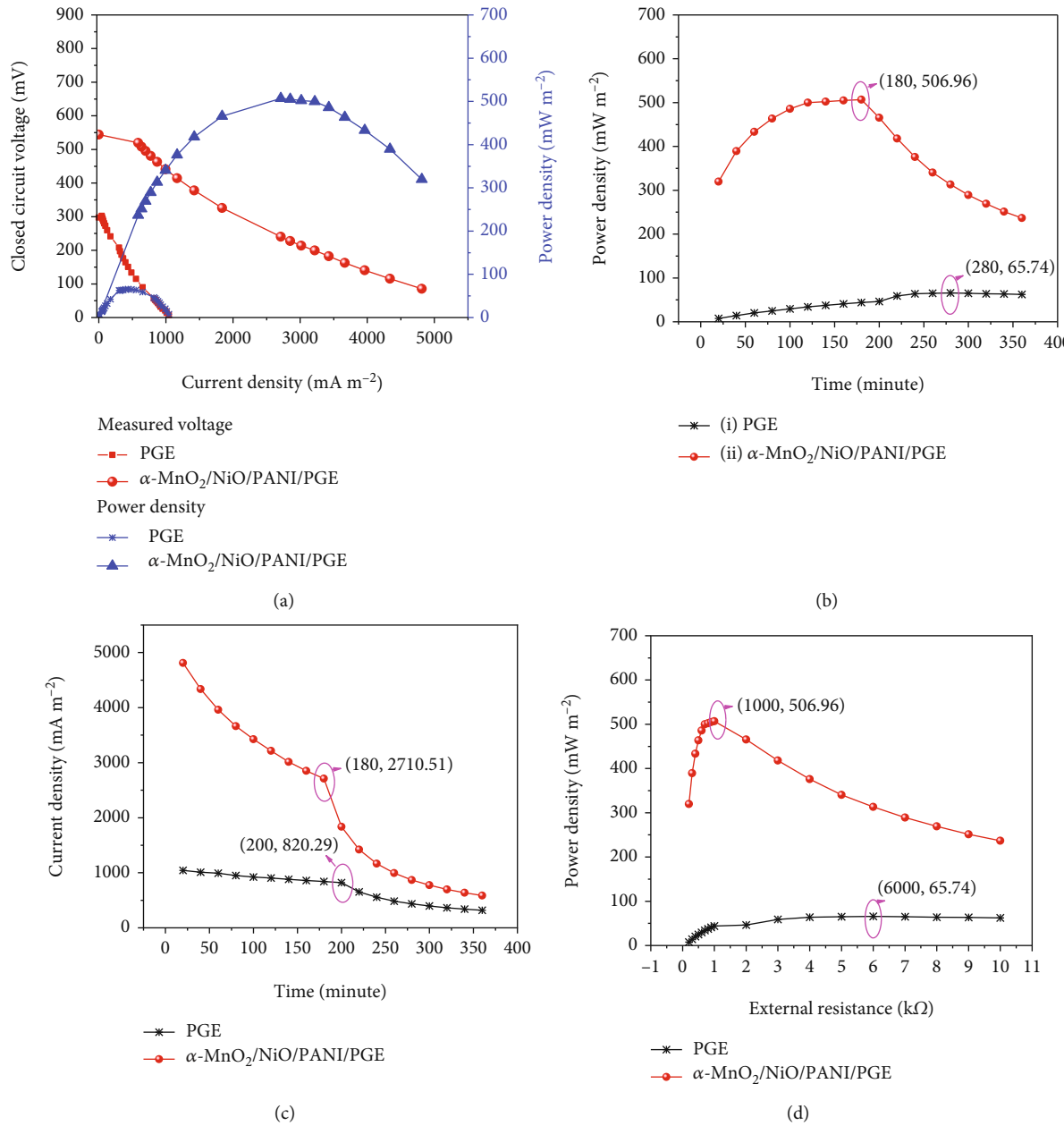

Figure 12: Power density and polarization curves (a), power density versus time (b), current density versus time (c), and power density dependence external load (d) for PGE and α-MnO_2/NiO/PANI/PGE.

topography of bare PGE is shown in Figure 13(a). The roughness of this surface is attributed to the granularity of the conductive materials [58]. After PGE is immersed in the anode bioreactor, the surface morphology of PGE is clearly covered by small colonies of *E. coli* which forms a biofilm due to the little hydrophilicity nature of bare PGE, as shown in Figure 13(b). However, such adherence of *E. coli* on the PGE surface was ineffective for power generation during MFC operations. This is due to the poor capacitive and little substrate degradation activity of carbon electrode materials in MFC performance [10]. So, to solve these limitations, bare PGE was successfully modified with α-MnO_2/NiO/PANI ternary composites. As shown in Figure 13(c), the integration between α-MnO_2/NiO binary composites in the conductive PANI matrix exhibited a higher bacterial colony. It is observed that the distribution of bimetallic oxide with positively charged PANI enhances the glucose electrochemical reactions. Such reaction was enabled to facilitate better power production than bare PGE, as described from the MFC test analysis. This is due to the formation of thick conductive biofilm as evidenced from the high-magnification surface topography view, as shown in Figures 13(d) and 13(e). From this magnified image, *E. coli* cells are tightly attached to the modified anode surface to form the bioanode electrode. Xu et al. [59] have reported that when a bare carbon electrode is modified by conductive composites from PANI, its surface roughness and biocompatibility are increased, which makes it more comfortable for more biofilms to attach, helping it

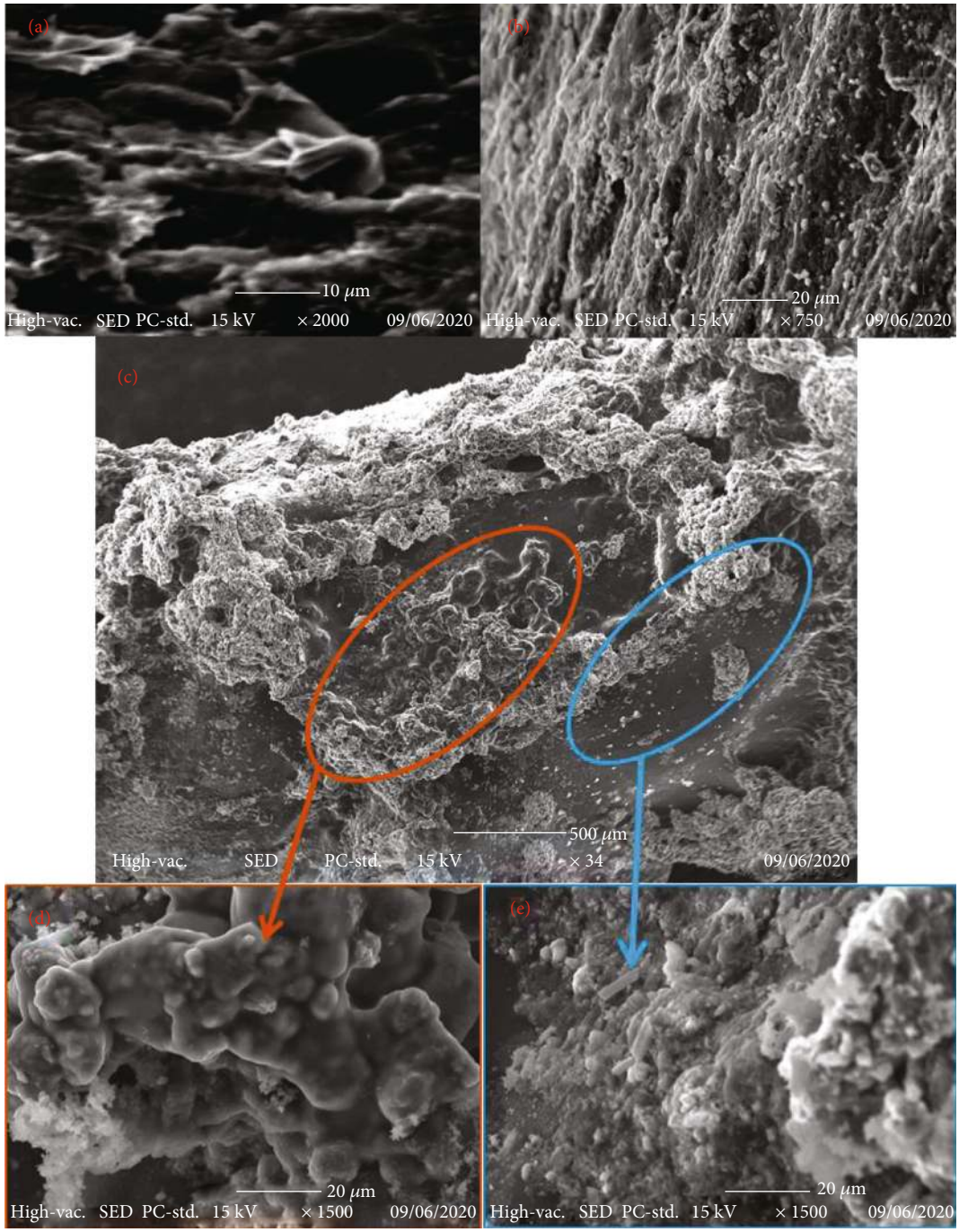

Figure 13: SEM micrograph of bare PGE (a), biocatalyst-modified PGE (b), α-MnO_2/NiO/PANI composite-modified PGE (c), and composite-modified electrodes at high resolution (d, e).

become more conductive [59]. Finally, this enabled the creation of a direct electron transfer improvement between *E. coli* outer membrane c-type cytochromes and α-MnO_2/NiO/-PANI/PGE for better MFC performance operation.

3.10. COD Removal and CE Performance. In addition to generating electricity, treating glucose-based artificial wastewater using bare PGE and α-MnO_2/NiO/PANI-modified PGE is shown in Figures 14(a) and 14(b). It is observed that the higher glucose degradation performance was performed with a lower concentration and higher removal efficiency of 30.37 $mg\,L^{-1}$ and 81.92%, respectively, using α-MnO_2/NiO/PA-NI/PGE. Degradation efficiency using bare PGE was too low due to the slower glucose biodegradation rate, indicating less COD removal efficiency over a given time period. Thus, electron transfer from decomposed glucose to the bare anode is too slow while faster in α-MnO_2/NiO/PANI ternary composite-modified PGE due to their surface modification. To support this, the degree (fraction) of electrons produced from glucose to modified PGE was higher in terms of CE with

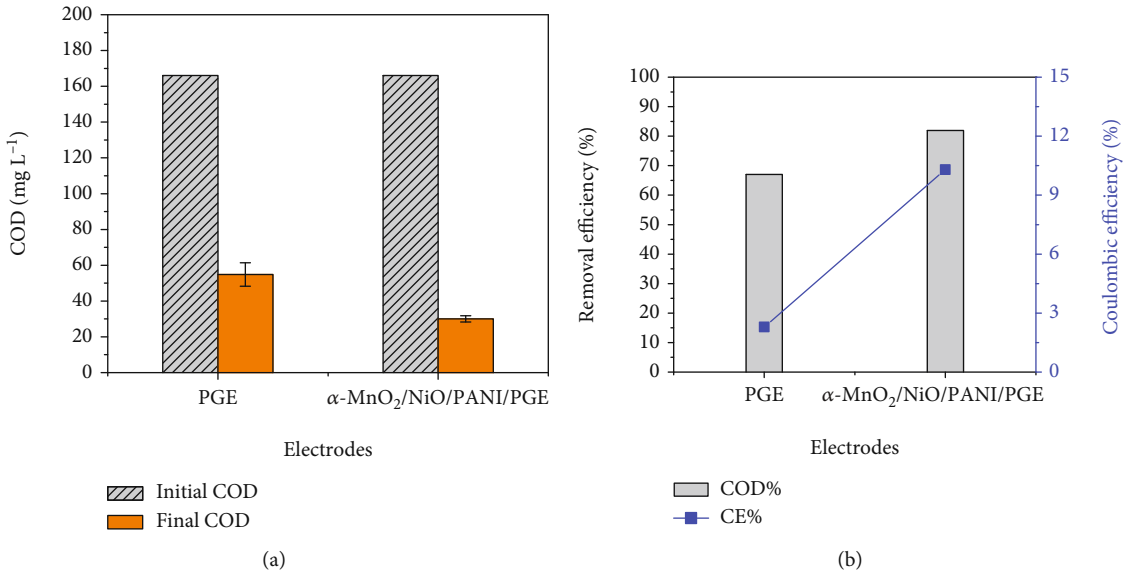

Figure 14: (a) Concentration and (b) removal efficiency performances using bare PGE and α-MnO_2/NiO/PANI-modified PGE under closed-circuit conditions.

Table 10: Summary of triplicate final concentration (COD_f) and their COD removal efficiency values for different anode electrodes during CCV measurements under optimum conditions.

Anode electrode	Experiment 1 (COD_f (mg L^{-1}))	Experiment 2 (COD_f (mg L^{-1}))	Experiment 3 (COD_f (mg L^{-1}))	Mean ± SD (mg L^{-1})	Removal efficiency (COD%)	Coulombic efficiency (CE%)
PGE	50.92	51.20	62.39	54.84 ± 6.54	67.00	2.29
α-MnO_2/NiO/PANI/PGE	31.59	28.10	30.37	30.02 ± 1.77	81.92	10.30

(Mean ± SD) is calculated using OriginPro 8 software. SD = standard deviation; substrate = (glucose, COD_o, 166 mg/L). *Note*: both COD removal efficiency and CE were calculated from the mean values of COD_f.

a value of 10.30% while PGE alone has a small CE value of 2.29%, as shown in Figure 14(b) and Table 10. The faster electron transfer using ternary composite-modified PGE was also effective in bioelectricity generation conversion during the time of treatment at the same conditions. Literature survey described that the lower CE values have indicated that a portion of electrons extracted from substrates are used for the biosynthesis of cellular compounds, not for complete bioelectricity production, whereas higher CE would indicate the dominance of bioelectricity conversion rather than for biosynthesis [60].

4. Conclusion

α-MnO_2/NiO/PANI ternary composites are prepared by dispersing the optimized biosynthesized α-MnO_2/NiO bimetallic NPs in the conductive PANI matrix using the *in situ* chemical polymerization method. The prepared ternary composites showed to be best in the degree of roughness and charge storing performances with a value of 23.65 ± 5.652 nm and 24.456 mC. This property clearly increases the biocompatibility, electrical conductivity, and life cycle of the anode in MFC by improving its performance towards a maximum power density of 506.96 mW m^{-2} with a COD removal of 81.92%. The power density produced by the α-MnO_2/NiO/PANI ternary composite-modified anode is better in efficiency than power output which was done by biosynthesized α-MnO_2/NiO bimetallic NPs with a mean value of 412.24 mW m^{-2} [21]. The CE produced by the α-MnO_2/NiO/PANI/PGE ternary composite was 10.30% which was almost 5-fold better than bare PGE with a value of 2.29%. Therefore, this study contributes to advances in the use of biosynthesized α-MnO_2/NiO-based PANI ternary composites as an emerging cost-effective catalyst for anode modifier catalysts in energy conversion and simultaneous wastewater treatment application in MFC.

Data Availability

Data are available in the manuscript.

Conflicts of Interest

The authors declare no conflict of interest in this paper.

Acknowledgments

The authors acknowledge Adama Science and Technology University for financial support.

References

[1] A. Parkash, "Microbial fuel cells: a source of bioenergy," *Journal of Microbial and Biochemical Technology*, vol. 8, no. 3, pp. 247–255, 2016.

[2] X. Zhao, T. Tian, M. Guo, X. Liu, and X. Liu, "Cauliflower-like polypyrrole@MnO2 modified carbon cloth as a capacitive anode for high-performance microbial fuel cells," *Journal of Chemical Technology and Biotechnology*, vol. 95, no. 1, pp. 163–172, 2020.

[3] Y. Dessie, S. Tadesse, and R. Eswaramoorthy, "Review on manganese oxide based biocatalyst in microbial fuel cell: nanocomposite approach," *Materials Science in Energy Technology*, vol. 3, pp. 136–149, 2020.

[4] Y. Dessie, S. Tadesse, R. Eswaramoorthy, and B. Abebe, "Recent developments in manganese oxide based nanomaterials with oxygen reduction reaction functionalities for energy conversion and storage applications: a review," *Journal of Science: Advanced Materials and Devices*, vol. 4, no. 3, pp. 353–369, 2019.

[5] H. Xu, X. Quan, Z. Xiao, and L. Chen, "Effect of anodes decoration with metal and metal oxides nanoparticles on pharmaceutically active compounds removal and power generation in microbial fuel cells," *Chemical Engineering Journal*, vol. 335, no. August 2017, pp. 539–547, 2018.

[6] Y. Qiao, X. S. Wu, and C. M. Li, "Interfacial electron transfer of _Shewanella putrefaciens_ enhanced by nanoflaky nickel oxide array in microbial fuel cells," *Journal of Power Sources*, vol. 266, pp. 226–231, 2014.

[7] X. Wan, S. Yang, Z. Cai et al., "Facile synthesis of MnO2 nanoflowers/N-doped reduced graphene oxide composite and its application for simultaneous determination of dopamine and uric acid," *Nanomaterials*, vol. 9, no. 6, p. 847, 2019.

[8] S. Mathew and P. C. Thomas, "Fabrication of polyaniline nanocomposites as electrode material for power generation in microbial fuel cells," *Materials Today: Proceedings*, vol. 33, pp. 1415–1419, 2020.

[9] S. Shivakumara and N. Munichandraiah, "In-situ preparation of nanostructured α-MnO_2/polypyrrole hybrid composite electrode materials for high performance supercapacitor," *Journal of Alloys and Compounds*, vol. 787, pp. 1044–1050, 2019.

[10] D. Zhong, X. Liao, Y. Liu, N. Zhong, and Y. Xu, "Enhanced electricity generation performance and dye wastewater degradation of microbial fuel cell by using a petaline polyaniline-carbon felt anode," *Bioresource Technology*, vol. 258, no. November 2017, pp. 125–134, 2018.

[11] H. K. Inamdar, R. B. Basavaraj, H. Nagabhushana et al., "DC conductivity study of polyaniline/NiO nanocomposites prepared through green synthesis," *Materials Today: Proceedings*, vol. 3, no. 10, pp. 3850–3854, 2016.

[12] J. He, M. Wang, W. Wang et al., "Hierarchical mesoporous NiO / MnO 2 @ PANI core- shell microspheres highly efficient and stable bifunctional electrocatalysts for oxygen evolution and reduction reactions," *ACS Applied Materials & Interfaces*, vol. 9, no. 49, pp. 42676–42687, 2017.

[13] O. E. Fayemi, A. S. Adekunle, and E. E. Ebenso, "Electrochemical detection of phenanthrene using nickel oxide doped PANI nanofiber based modified electrodes," *Journal of Nanomaterials*, vol. 2016, Article ID 9614897, 12 pages, 2016.

[14] F. Nourbakhsh, M. Mohsennia, and M. Pazouki, "Nickel oxide/carbon nanotube/polyaniline nanocomposite as bifunctional anode catalyst for high-performance Shewanella-based dual-chamber microbial fuel cell," *Bioprocess and Biosystems Engineering*, vol. 40, no. 11, pp. 1669–1677, 2017.

[15] T. H. Han, N. Parveen, J. H. Shim, A. T. N. Nguyen, N. Mahato, and M. H. Cho, "Ternary composite of polyaniline graphene and TiO2as a bifunctional catalyst to enhance the performance of both the bioanode and cathode of a microbial fuel cell," *Industrial and Engineering Chemistry Research*, vol. 57, no. 19, pp. 6705–6713, 2018.

[16] C. Zhao, P. Gai, C. Liu et al., "Polyaniline networks grown on graphene nanoribbons-coated carbon paper with a synergistic effect for high-performance microbial fuel cells," *Journal of Materials Chemistry A*, vol. 1, no. 40, pp. 12587–12594, 2013.

[17] W. Chen, Z. Liu, G. Su et al., "Composite-modified anode by MnO2/polypyrrole in marine benthic microbial fuel cells and its electrochemical performance," *International Journal of Energy Research*, vol. 41, no. 6, pp. 845–853, 2017.

[18] Y. Wang, Q. Wen, Y. Chen, and L. Qi, "A novel polyaniline interlayer manganese dioxide composite anode for high- performance microbial fuel cell," *Journal of the Taiwan Institute of Chemical Engineers*, vol. 75, pp. 112–118, 2017.

[19] H. Yuan, L. Deng, Y. Chen, and Y. Yuan, "MnO_2/polypyrrole/MnO_2 multi- walled-nanotube-modified anode for high-performance microbial fuel cells," *Electrochimica Acta*, vol. 196, pp. 280–285, 2016.

[20] P. Mishra and R. Jain, "Electrochemical deposition of MWCNT-MnO_2/PPy nano- composite application for microbial fuel cells," *International Journal of Hydrogen Energy*, vol. 41, no. 47, pp. 22394–22405, 2016.

[21] Y. Dessie, S. Tadesse, R. Eswaramoorthy, and E. Abdisa, "Bimetallic Mn-Ni oxide nanoparticles: green synthesis, optimization and its low-cost anode modifier catalyst in microbial fuel cell," *Nano-Structures and Nano-Objects*, vol. 25, article 100663, 2021.

[22] Y. Dessie, S. Tadesse, and R. Eswaramoorthy, "Physicochemical parameter influences and their optimization on the biosynthesis of MnO_2 nanoparticles using _*Vernonia amygdalina*_ leaf extract," *Arabian Journal of Chemistry*, vol. 13, no. 8, pp. 6472–6492, 2020.

[23] M. R. Mohammad Shafiee, A. Sattari, M. Kargar, and M. Ghashang, "MnO2/Cr2O3/PANI nanocomposites prepared byin situoxidation polymerization method: optical and electrical behaviors," *Journal of Applied Polymer Science*, vol. 136, no. 15, article 47219, 2019.

[24] M. Harshiny, N. Samsudeen, R. J. Kameswara, and M. Matheswaran, "Biosynthesized FeO nanoparticles coated carbon anode for improving the performance of microbial fuel cell," *International Journal of Hydrogen Energy*, vol. 42, no. 42, pp. 26488–26495, 2017.

[25] Madhusudhana, G. Manasa, A. K. Bhakta, Z. Mekhalif, and R. J. Mascarenhas, "Bismuth-nanoparticles decorated multiwall-carbon-nanotubes cast-coated on carbon paste electrode; an electrochemical sensor for sensitive determination of gallic acid at neutral pH," *Materials Science in Energy Technology*, vol. 3, pp. 174–182, 2020.

[26] S. Kalathil, V. H. Nguyen, J. J. Shim, M. M. Khan, J. Lee, and M. H. Cho, "Enhanced performance of a microbial fuel cell using CNT/MnO_2 nanocomposite as a bioanode material," *Journal of Nanoscience and Nanotechnology*, vol. 13, no. 11, pp. 7712–7716, 2013.

[27] S. Patade, K. Silveira, A. Babu et al., "Bioremediation of dye effluent waste through an optimised microbial fuel cell,"

International Journal of Advanced Research in Biological Sciences, vol. 3, no. 3, pp. 214–226, 2016.

[28] M. Danish Khan, H. Abdulateif, I. M. Ismail, S. Sabir, and M. Zain Khan, "Bioelectricity generation and bioremediation of an azo-dye in a microbial fuel cell coupled activated sludge process," *PLoS One*, vol. 10, no. 10, 2015.

[29] S. Pandit, S. Khilari, S. Roy, D. Pradhan, and D. Das, "Improvement of power generation using _Shewanella putrefaciens_ mediated bioanode in a single chambered microbial fuel cell: effect of different anodic operating conditions," *Bioresource Technology*, vol. 166, pp. 451–457, 2014.

[30] M. Kloch and R. Toczylowska-Maminska, "Toward optimization of wood industry wastewater treatment in microbial fuel cells-mixed wastewaters approach," *Energies*, vol. 13, no. 1, p. 263, 2020.

[31] R. S. Diggikar, S. P. Deshmukh, T. S. Thopate, and S. R. Kshirsagar, "Performance of polyaniline nanofibers (PANI NFs) as PANI NFs-silver (Ag) nanocomposites (NCs) for energy storage and antibacterial applications," *ACS Omega*, vol. 4, no. 3, pp. 5741–5749, 2019.

[32] S. Ahmad, M. M. Ali Khan, and F. Mohammad, "Graphene/-nickel oxide-based nanocomposite of polyaniline with special reference to ammonia sensing," *ACS Omega*, vol. 3, no. 8, pp. 9378–9387, 2018.

[33] A. P. Mahajan, S. B. Kondawar, R. P. Mahore, B. H. Meshram, and P. D. Virutkar, "Polyaniline/MnO_2 nanocomposites based stainless steel electrode modified enzymatic urease biosensor," *Procedia Materials Science*, vol. 10, pp. 699–705, 2015.

[34] X. Zhou, Y. Xu, X. Mei et al., "Polyaniline/β-MnO_2 nanocomposites as cathode electrocatalyst for oxygen reduction reaction in microbial fuel cells," *Chemosphere*, vol. 198, pp. 482–491, 2018.

[35] A. Angel Ezhilarasi, J. Judith Vijaya, K. Kaviyarasu, L. John Kennedy, R. J. Ramalingam, and H. A. Al-Lohedan, "Green synthesis of NiO nanoparticles using _*Aegle marmelos*_ leaf extract for the evaluation of in-vitro cytotoxicity, antibacterial and photocatalytic properties," *Journal of Photochemistry and Photobiology B: Biology*, vol. 180, pp. 39–50, 2018.

[36] Z. Hu, L. Zu, Y. Jiang et al., "High specific capacitance of polyaniline/mesoporous manganese dioxide composite using KI-H2SO4 electrolyte," *Polymers*, vol. 7, no. 10, pp. 1939–1953, 2015.

[37] M. O. Ansari, M. M. Khan, S. A. Ansari, K. Raju, J. Lee, and M. H. Cho, "Enhanced thermal stability under DC electrical conductivity retention and visible light activity of Ag/TiO2@-polyaniline nanocomposite film," *ACS Applied Materials & Interfaces*, vol. 6, no. 11, pp. 8124–8133, 2014.

[38] S. A. Ansari, N. Parveen, T. H. Han, M. O. Ansari, and M. H. Cho, "Fibrous polyaniline@manganese oxide nanocomposites as supercapacitor electrode materials and cathode catalysts for improved power production in microbial fuel cells," *Physical Chemistry Chemical Physics*, vol. 18, no. 13, pp. 9053–9060, 2016.

[39] M. O. Ansari and F. Mohammad, "Thermal stability of HCl-doped-polyaniline and TiO 2 nanoparticles-based nanocomposites," *Journal of Applied Polymer Science*, vol. 124, no. 6, pp. 4433–4442, 2012.

[40] R. Taş, M. Can, and S. Sönmezoğlu, "Preparation and characterization of polyaniline microrods synthesized by using dodecylbenzene sulfonic acid and periodic acid," *Turkish Journal of Chemistry*, vol. 39, no. 3, pp. 589–599, 2015.

[41] R. Djara, Y. Holade, A. Merzouki et al., "Insights from the physicochemical and electrochemical screening of the potentiality of the chemically synthesized polyaniline," *Journal of the Electrochemical Society*, vol. 167, no. 6, article 066503, 2020.

[42] S. Nasrazadani and S. Hassani, "Modern analytical techniques in failure analysis of aerospace, chemical, and oil and gas industries," in *Handbook of Materials Failure Analysis with Case Studies from the Oil and Gas Industry*, pp. 39–54, Elsevier, 2016.

[43] J. Rudloff-Grund, F. E. Brenker, K. Marquardt, F. V. Kaminsky, and A. Schreiber, "STEM EDX nitrogen mapping of nanoinclusions in milky diamonds from Juina, Brazil, using a windowless silicon drift detector system," *Analytical Chemistry*, vol. 88, no. 11, pp. 5804–5808, 2016.

[44] Z. Ye, J. Hou, M. W. Ellis, and B. Behkam, "Effect of anode surface roughness on power generation in microbial fuel cells," in *Vol. 6 Energy, Parts A B, American Society of Mechanical Engineers*, pp. 1409–1414, 2012.

[45] S. Zhao, Y. Li, Y. Wang, Z. Ma, and X. Huang, "Quantitative study on coal and shale pore structure and surface roughness based on atomic force microscopy and image processing," *Fuel*, vol. 244, pp. 78–90, 2019.

[46] M. Hu, Z. Yao, and X. Wang, "Characterization techniques for graphene-based materials in catalysis," *AIMS Materials Science*, vol. 4, no. 3, pp. 755–788, 2017.

[47] P. Bhawal, S. Ganguly, T. K. Chaki, and N. C. Das, "Synthesis and characterization of graphene oxide filled ethylene methyl acrylate hybrid nanocomposites," *RSC Advances*, vol. 6, no. 25, pp. 20781–20790, 2016.

[48] A. B. Radwan, A. M. Abdullah, A. M. A. Mohamed, and M. A. Al-Maadeed, "New electrospun polystyrene/Al2O3 nanocomposite superhydrophobic coatings; synthesis, characterization, and application," *Coatings*, vol. 8, no. 2, 2018.

[49] S. Ou, H. Kashima, D. S. Aaron, J. M. Regan, and M. M. Mench, "Full cell simulation and the evaluation of the buffer system on air-cathode microbial fuel cell," *Journal of Power Sources*, vol. 347, pp. 159–169, 2017.

[50] D. He, E. Rauwel, R. Malpass-Evans et al., "Redox reactivity at silver microparticle—glassy carbon contacts under a coating of polymer of intrinsic microporosity (PIM)," *Journal of Solid State Electrochemistry*, vol. 21, no. 7, pp. 2141–2146, 2017.

[51] S. Tahtaisleyen, O. Gorduk, and Y. Sahin, "Electrochemical determination of sunset yellow using an electrochemically prepared graphene oxide modified – pencil graphite electrode (EGO-PGE)," *Analytical Letters*, vol. 54, no. 3, pp. 394–416, 2021.

[52] S. u. Haque, A. Nasar, Inamuddin, and M. M. Rahman, "Applications of chitosan (CHI)-reduced graphene oxide (rGO)-polyaniline (PAni) conducting composite electrode for energy generation in glucose biofuel cell," *Scientific Reports*, vol. 10, no. 1, article 10428, 2020.

[53] Z. Qin, J. Zhang, Y. Liu et al., "A simple but efficient voltammetric sensor for simultaneous detection of tartrazine and ponceau 4R based on TiO2/electro-reduced graphene oxide nanocomposite," *Chemosensors*, vol. 8, no. 3, p. 70, 2020.

[54] H. Yin, S. Ai, W. Shi, and L. Zhu, "A novel hydrogen peroxide biosensor based on horseradish peroxidase immobilized on gold nanoparticles-silk fibroin modified glassy carbon electrode and direct electrochemistry of horseradish peroxidase," *Sensors and Actuators B: Chemical*, vol. 137, no. 2, pp. 747–753, 2009.

[55] R. Ramachandran, W. Xuan, C. Zhao et al., "Enhanced electrochemical properties of cerium metal-organic framework based composite electrodes for high-performance supercapacitor application," *RSC Advances*, vol. 8, no. 7, pp. 3462–3469, 2018.

[56] H. Gebretinsae, G. Welegergs, N. Matinise, M. Maazab, and Z. Y. Nurua, "Electrochemical study of nickel oxide (NiO) nanoparticles from cactus plant extract," *MRS Advances*, vol. 5, no. 21–22, pp. 1095–1102, 2020.

[57] M. Ghasemi, W. R. W. Daud, M. Rahimnejad et al., "Copper-phthalocyanine and nickel nanoparticles as novel cathode catalysts in microbial fuel cells," *International Journal of Hydrogen Energy*, vol. 38, no. 22, pp. 9533–9540, 2013.

[58] K. Skrzypczynska, K. Kusmierek, A. Swiatkowski, and L. Dabek, "The influence of pencil graphite hardness on voltammetric detection of pentachlorophenol," *International Journal of Electrochemical Science*, vol. 13, no. 1, pp. 88–100, 2018.

[59] H. Xu, L. Wang, C. Lin et al., "Improved simultaneous decolorization and power generation in a microbial fuel cell with the sponge anode modified by polyaniline and chitosan," *Applied Biochemistry and Biotechnology*, vol. 192, no. 2, pp. 698–718, 2020.

[60] Z. A. Stoll, J. Dolfing, and P. Xu, "Minimum performance requirements for microbial fuel cells to achieve energy-neutral wastewater treatment," *Watermark*, vol. 10, no. 3, p. 243, 2018.